Universidade Federal do Rio Grande do Sul
Programa de Pós-Graduação em Física
Tese de Doutorado

Wetting Phenomena: from basic science to applications

Estudo da fenomenologia de molhabilidade: da ciencia básica às aplicações

Marion Lucia Silvestrini

Orientadora: Carolina Brito

December 2021

Estudo da fenomenologia de molhabilidade: da ciência básica às aplicações

Aluna: Marion Silvestrini
Orientadora: Carolina Brito

Resumo (press release)

Molhabilidade é o estudo do comportamento de líquidos sobre superfícies sólidas. Esta área tem inúmeras aplicações, como por exemplo a criação de roupas impermeáveis com superfícies que repelem água e óleo (hidrofóbica e oleofóbica, respectivamente) ou fraldas descartáveis usando superfícies que absorvem os líquidos (hidrofílica/oleofílica). Um dos problemas centrais nesta área é entender o fenômeno de *metaestabilidade*: dependendo de como a gota é depositada, ela pode molhar ou ser repelida pela superfície. Este tipo de problema importa tanto na física básica quanto para construir superfícies super-repelentes ou que absorvam bem a água na atmosfera. Neste trabalho usamos um modelo teórico e simulações para destrinchar este fenômeno e entender os parâmetros da superfície para que ocorra ou não a metaestabilidade.

A figura 1 contém um exemplo das nossas simulações. No trabalho entendemos em que casos a superfície apresenta metaestabilidade e exploramos as limitações dos modelos teóricos que são incapazes de prever mais de um estado de molhabilidade para cada superfície.

Outro aspecto abordado na tese é de interesse sócio ambiental: para quais superfícies é possível separar uma mistura de água e óleo usando suas propriedades de molhabilidade? A figura 2 mostra uma gota com água e óleo em uma superfície que age como uma esponja: simultaneamente absorve o óleo (oleofílica) e repele a água (hidrofóbica). Nós estudamos numérica e teoricamente quais as geometrias que permitem uma separação mais eficiente.

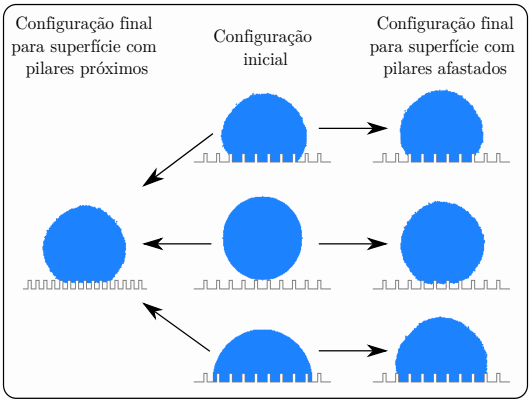

Figura 1: Coluna central mostra três exemplos de condições iniciais (configurações de gota usadas no início da simulação). Coluna à esquerda: independente da condição inicial, o estado final da gota sobre a superfície com pilares próximos é sempre hidrofóbico. Coluna à direita: para cada condição inicial, a gota se comporta de uma maneira diferente quando está depositada sobre pilares mais espaçados.

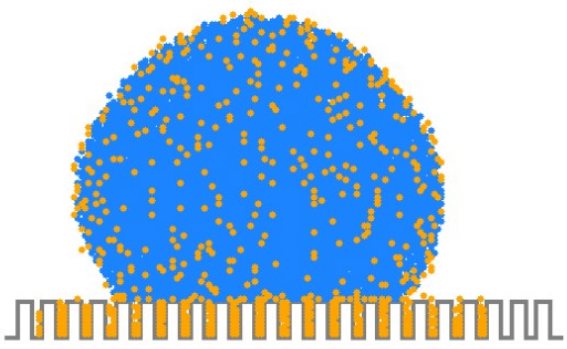

Figura 2: Exemplo de superfície oleofílica e hidrofóbica.

Abstract

The study of wetting phenomena in solids is of great interest due to the multifaceted technological applications of hydrophobic, hydrophilic and oleophobic surfaces. Examples of such applications include self cleaning materials and water purifying surfaces. Besides the applications, there are still fundamental open questions concerning the transition between the wet and dry surface states, such as the existence of metastable states and their features. In this thesis we apply a theoretical approach, based on calculating the interfacial energy cost of different configurations to study wetting phenomena. We initially apply this method to predict the wetting states and contact angles of droplets placed on a specific surface; this approach guides us to select a relevant parameter set for further analysis. Then, we use a Monte Carlo simulation of the cellular Potts model, with the selected parameters, for two different purposes: the first is calculating the free energy profile of a liquid droplet deposited on a pillared surface. In this study, we show that there is only one minimum of the free energy that corresponds to the superhydrophobic wetting state while the wet state can present multiple minima. The second purpose is calculating the efficiency in separating water and oil. By analyzing different substrates, we found that the separation efficiency depends on the surface parameters. Moreover, we observe that for a droplet composed of water and oil, the water behavior can be predicted by the theoretical approach, while the oil behaves in a more complex manner, partially due to the formation of a oil film in the interface of the droplet with the air. We believe that our results may elucidate some of the open question in the field of wetting phenomena and rare events.

Resumo

O estudo da fenomenologia de molhabilidade em sólidos é de grande interesse devido às múltiplas aplicações tecnológicas de superfícies hidrofóbicas, hidrofílicas e oleofóbicas. Exemplos de tais aplicações incluem materiais auto-limpantes e superfícies capazes de purificar água. Além das aplicações, ainda existem dúvidas fundamentais quanto a transição entre os estados secos e molhados da superfície, como a existência de estados metaestáveis. Nesta tese aplicamos um método teórico para estudar a fenomenologia de molhabilidade. Inicialmente aplicamos este método para prever o estado molhado e o angulo de contato de gotas colocadas sobre superfícies específicas; esta abordagem nos guia para selecionar conjuntos de parâmetros relevantes para melhor analisá-los posteriormente. Então, usamos simulações de Monte Carlo do modelo celular de Potts, com os parâmetros escolhidos, para dois objetivos: no primeiro calculamos o perfil de energia livre de uma gota depositada sobre uma superfície de pilares. Neste estudo concluímos que existe apenas um mínimo na energia livre correspondente ao estado hidrofóbico enquanto que o estado hidrofílico pode apresentar múltiplos mínimos. O segundo objetivo é calcular a eficiência de separação da mistura água e óleo. Analisando diferentes superfícies, descobrimos que a eficácia de separação depende dos parâmetros da superfície. Além disso, observamos que, para uma gota composta de ambos líquidos, o comportamento da água pode ser previsto pelo método teórico, enquanto que o óleo se comporta de uma maneira complexa, parcialmente devido à formação de um filme de óleo na interface da gota com o ar. Acreditamos que nossos resultados possam esclarecer algumas das questões em abertos na área de molhabilidade e eventos raros.

Agradecimentos

Gostaria de expressar meus mais profundos agradecimentos para as pessoas que foram importantes para mim e estiveram me apoiando durante os últimos anos.

Ao meus pais, Beatriz e Jorge, que estiveram comigo nessa jornada acadêmica desde sempre, me ajudando a aprender, desde derivada e integral até métodos computacionais e linguagem de programação. Meu irmão, Nahuel, que me ajudou a tomar decisões importantes e a ter confiança nessas escolhas. Laura, minha cunhada, é das pessoas mais tranquilas que eu conheço, característica que eu sempre tento espelhar, principalmente nos momentos de estresse (que foram diversos nos últimos meses). Também não poderia deixar de agradecer aos dois pelo presente que é minha sobrinha, Alicia, que mesmo morando tão longe está nos meus pensamentos todos os dias.

Agradeço imensamente a minha orientadora, Carolina Brito, que é um modelo para mim, tanto de cientista quanto de mulher. Em momentos que, às vezes, eu mesma duvidava do meu trabalho, a Carolina sempre me fez ter confiança em mim e nos nossos resultados. Também agradeço profundamente ao grupo de pesquisa, por me propiciar discussões interessantes e me ajudar em momentos de dificuldade. Trabalhar juntamente com a Cristina, o Davi e o Fábio foi um prazer enorme, que eu espero repetir futuramente.

Stefanie, Roberta, Ana Maria, Camila e Bruna são algumas das mulheres que tive o privilégio de conhecer há mais de uma década e manter uma amizade muito bonita. Tenho muito prazer de ter crescido com suas companhias e muito orgulho de ver as pessoas maravilhosas que elas se tornaram. Além disso, agradeço a todas as pessoas que conheci durante o período de faculdade, seja graduação ou pós-graduação. O convívio constante com pessoas diferentes me fez crescer como indivíduo, e entender diferentes pontos de vista.

Finalmente, deixo registrado um enorme agradecimento ao meu companheiro Rafael, que me sempre me incentivou a ir atrás dos meus desejos, me ajudou a lidar com calma e paciência os momentos de estresse durante todos esses anos, além de me ensinar a valorizar meus trabalhos. Também agradeço a sua família, Dilamar, Valdair, Aline e

Augusto, que sempre me receberam tão bem em suas casas e me fizeram sentir parte da família.

List of Figures

Contents

Chapter 1

Introduction

Thomas Young was a pioneer on the study of wetting properties of solid surfaces. In the 19th century, Young argumented that the contact angle (see definition in Figure 1.1-a) of a water droplet on top of an ideally flat surface is defined univocally by the surface tension σ_{IJ} between each pair of interfaces IJ: air-liquid, liquid-solid and air-solid [1].

More than a hundred years later, Robert Wenzel demonstrated that the *apparent* contact angle of a droplet on a textured surface (denoted by θ_{C}, see Figure 1.1-b) is in general different from θ_{Y} [2]. This distinction is important since it has consequences on the wetting properties of the solid. For instance, a rough solid may increase the contact angle as compared to the smooth solid, thus leading to more efficient repelling (or absorption) of the droplet. Figure 1.1-(a,b) shows a schematic drawing of a droplet on flat and rough surfaces, where $\theta_{\mathrm{Y}} < \theta_{\mathrm{C}}$.

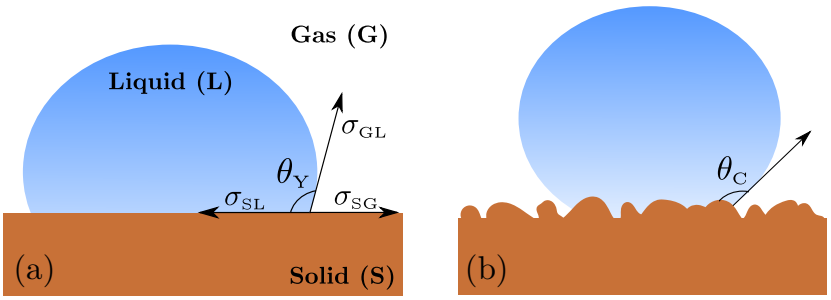

Figure 1.1: a water droplet on a **(a)** flat and **(b)** textured solid, presenting contact angles denoted by θ_{Y} and θ_{C} respectively. In the case displayed here, the roughness of the surface in **(b)** increases the hydrophobicity of the solid.

The equilibrium configuration of a droplet placed on a solid surface depends on various parameters, such as the topology of the surface, as discussed above. Besides that,

factors such as chemistry of the surface, type and volume of liquid can also change the droplet configuration [3, 4, 5, 6, 7, 8]. In the case of water the two extreme situations are known as hydrophilic state ($\theta_C < 90°$) and hydrophobic state ($\theta_C > 90°$). For a droplet of oil, this extrema are known as oleophobic (high θ_C) and oleophilic (low θ_C) states. The liquid-gas surface tension of the oil is much smaller than the value for water, which means that the oil tends to wet the surface more easily than the water.

There are interesting examples of this phenomena in nature. The particular case which motivated most research is the lotus leaf, see Figure 1.2-a. On panel **b** we show a microscopic view of the lotus surface and note that the roughness has a pillar-like shape at the microscale structure and also at a nanoscale structure [9]. This type of multiscale roughness is known to grant hydrophobic behavior to the surface. Another interesting example is the raft spider, an arachnid that has hydrophobic hair in the abdomen and legs, which permits the spider to walk on the water, Figure 1.2-c.

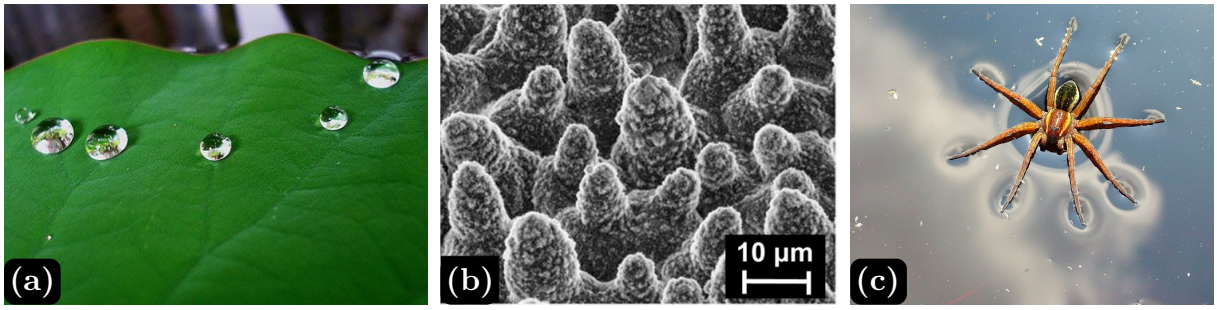

Figure 1.2: **(a)** lotus leaf with hydrophobic water droplets [10]. **(b)** microstructure of the lotus leaf [9]. **(c)** raft spider (*Dolomedes fimbriatus*) can walk on water due to its hydrophobic hair in the legs and abdomen [11].

Inspired by the appearance of hydrophobicity in nature, this phenomena have been applied also in technological applications. For example, coating a power cell with a layer of ultrahydrophobic material can increase the cell's efficiency [12]. It is possible to enhanced efficiency of submarines and ships using a similar idea, by coating them with a hydrophobic material. Other interesting applications of hydrophobicity are: self cleaning clothes, buildings or even surgical apparatus. On the other hand, hydrophilic surfaces are useful for ink printing [13, 14] and, in the biochemical area, useful to separate bacteria, virus or proteins [15].

For the particular case of oil, it was found a filefish, called *N. septentrionalis*, that can survive oil spills in the ocean because of its oleophobic skin. Instead of scales like most fish, this present a sandpapery bony skin. A microscopic scanning of the skin, Figure 1.3-b, shows the hook-like spines pattern with a slight deformation from the head (H) to the tail (T), responsible to make oil droplets roll from head to tail [16]. There are many

technological applications for this type of surface. For instance, an oleophobic coating can be useful to the textile industry, due to the self cleaning feature against several types of liquids [17, 18]. It can also be used to prevent oiliness on glasses and on the screens on smartphones [19]. This type of coating is already being used on surgical equipment to avoid accumulation of blood and bacteria, therefore preventing contamination [20].

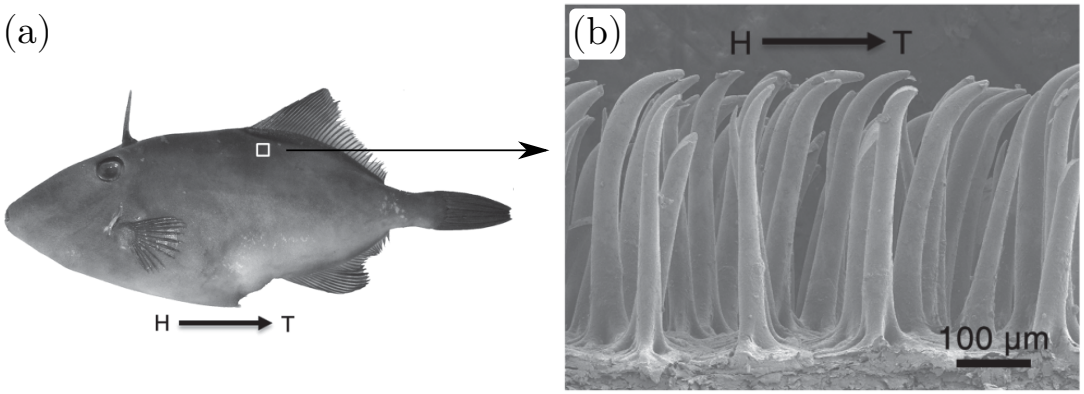

Figure 1.3: **(a)** photo of filefish *N. septentrionalis*. **(b)** microscopic side view of the white square in panel **(a)**. H denotes head and T denotes tail. Figure adapted from Reference [16].

In this thesis two aspects of the phenomenology described are studied: the characterization of the energy landscape for a droplet of water, article published in the Journal *Advanced Materials Interface* [21], and water-oil separation controlled by the topology of the surface, published in *The Journal of Chemical Physics* [22]. In the following we discuss both items and define the goals of each study.

From a purely thermodynamic standpoint, we cannot explain the existence of oleophobic surfaces. This means that these configurations do not arise in a global energy approach for liquids with low superficial tension, even if the geometry of the surface is manipulated [23]. The fact that oil droplets stay on top of carefully engineered surfaces tells us that there is an energy barrier determined by the kinetics of the process that separates the oleophobic and oleophilic states. In this sense, the oleophobic state is metastable and understanding its details is crucial to improve the technological development.

Metastability is a recurrent aspect of these type of systems and is also present in the case of water droplets. M. Callies *et al.* [5] showed in an experiment that external factors can alter the final configuration of a droplet. In this experiment, one droplet of water was placed carefully on the surface, while another identical droplet was thrown from a certain distance. The result was that the first stayed in a hydrophobic configuration with contact angle θ_1, Figure 1.4-a, while the latter assumed a hydrophilic configuration with contact angle θ_2, Figure 1.4-b. If we draw an sketch of the energy landscape for this system,

we would identify the hydrophobic state as a local minimum, the hydrophilic state as the global minimum and an energy barrier between them, Figure 1.4-c. Since these two droplets have different contact angles, we define a quantity called contact angle hysteresis (CAH) as the difference between them $\theta_H = |\theta_2 - \theta_1|$.

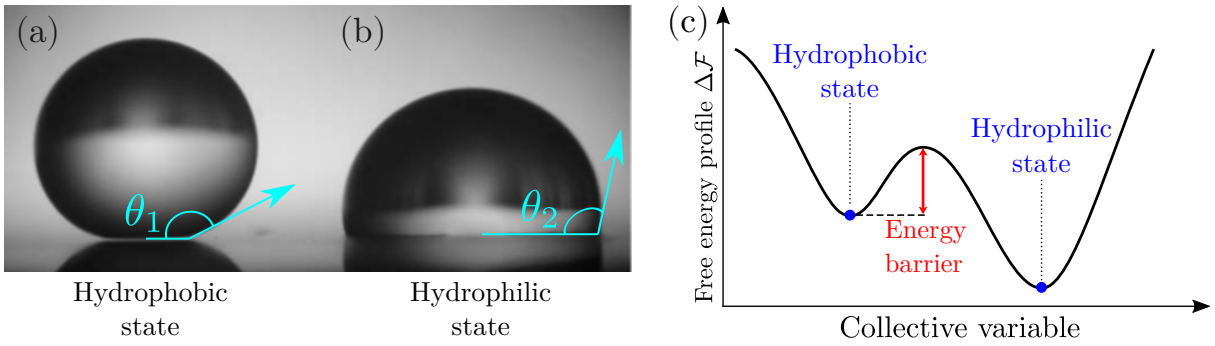

Figure 1.4: Example of metastability in a droplet of water. **(a)** Droplet was placed carefully in the surface. **(b)** Droplet thrown from a certain distance in the surface. Figure adapted from reference [5]. **(c)** Sketch of the energy landscape depicting a hydrophobic metastable state separated of the hydrophilic stable state by an energy barrier.

Simulating the transition between hydrophobic and hydrophilic states can be numerically challenging, since the observed time for such transitions can be of up to fifty days using high performance computers [24]. From these point of view, visiting completely the phase space can take a long time or never happen at all. A whole area of research is dedicated to the simulation of rare events [25, 26, 27, 28]. Depending on the system, metastable states can be exponentially numerous, and therefore it is not possible to assume that the phase space has been fully explored [29]. In the particular case of wettabillity, there are several studies pointing the need of further investigating of the metastable states [30, 31, 32]. Understanding the stability of hydrophobicity, and avoiding the transition to the hydrophilic state, is a crucial step which may have a large technological impact.

Due to the numerical challenge to fully explore this type of simulation, the analysis of the free energy landscape connected to wetting of a realistic surface by a droplet is still lacking. In this thesis we try to fill such a gap, providing a generic framework for reconstructing the free energy connected to wetting of a pillared surface based on the combination of the cellular Potts model and the string method for rare events. In addition, we employ a theoretical model, to calculate the thermodynamic stable state of a droplet on a rough surface. The two *homogeneous* wetting configurations analyzed with this approach are: Cassie-Baxter (CB), shown in Figure 1.5-a, defined as having the droplet rest on the surface, forming air pockets below the drop, and Wenzel (W), shown in Figure 1.5-b, characterized by the uniform wetting of the entire surface. Due to the homogeneity of the wetting states, we refer to this model as *homogenized approach*. The combination of

the two methods (homogenized approach and MC simulations) allows us to demonstrate that the free energy presents multiple minima and to verify the energetic origin of the hydrophobicity of the CB state. In addition, the presented approach provides useful guidelines for contact angle measurements on actual surfaces and for designing surfaces with tailored wetting properties, notably hydrophobic ones. The results of this study, published in the Journal *Advanced Materials Interface* [21], are discussed in Chapter 3.

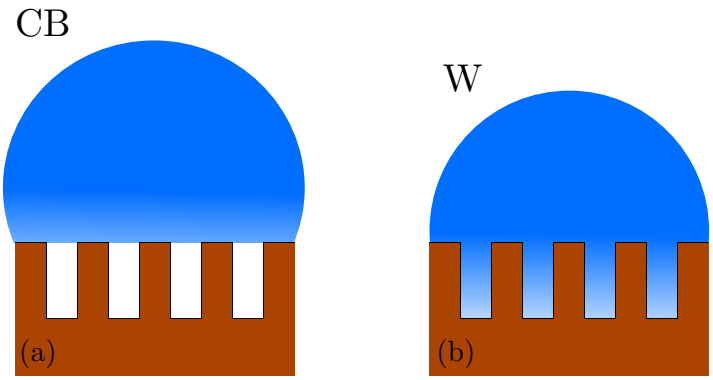

Figure 1.5: Scheme of theoretical wetting states: **(a)** Cassie-Baxter (CB) and **(b)** Wenzel (W) on the right.

Due to climate emergency, water desalinization [33, 34, 35] and water-oil separation [36, 37, 38] have been widely studied in order to obtain potable water. Particularly, there is an increase level of attention focused in oil-water separation techniques mainly due to oil been one of the most common pollutant in the world, principally from oil spill accidents and industry oily wastewater. Some of the conventional techniques used to separate this water-oil emulsions (droplets with diameter lower than $20\,\mu$m) are chemical emulsification [39], centrifugation [40], heat treatment [41] and membrane filtration [34]. Limitations of these conventional approaches includes high energy costs, operating costs, sludge production and limited efficiency [38]. Recently the role of wettability has been studied in order to propose more efficient and low costs water/oil separation methods. The idea is that by controlling the parameters of the surface is possible to engineer a material with antagonistic wetting behavior for oil and water that propitiates the mixture separation.

Despite the advances in this field, most studies are focused in the fabrication and performance of these materials and not in the underlying mechanisms that propitiate water/oil separation [42]. Therefore, more fundamental research toward understanding the interactions between water, oil and surfaces is extremely necessary in order to build a robust theoretical background that could be used as guideline for further developments in this area.

The homogenized approach is employed to calculate the stable state of a pure (water or oil) droplet on a textured surface, guiding us to select a set of surface parameters to further investigation. Then, to account for the water and oil interaction we also perform a Monte Carlo (MC) simulation of the 4-state cellular Potts model (CPM). This method allows us to study the separation capacity of a rough substrate and evaluate how the surface roughness affect the performance of these materials in separating oil from water. The goal of these studies is to fill the gap for the lack of theoretical work for water/oil separation using a wetting approach. The results of this study, published in *The Journal of Chemical Physics* [22], are discussed in Chapter 4.

This work is organized as follows: in Chapter 2 we present the analytical method and the numerical setup used: restrained Monte Carlo of the CPM combined with string method to study the metastable states in the case of pure water and the 4-state CPM to study the mixed water/oil droplet. Results and discussion for the free energy landscape are presented in Chapter 3 and for the water and oil separation are presented in Chapter 4. Finally, in Chapter 5 we draw conclusions and discuss the perspectives for future developments.

Chapter 2

Methods

In this chapter we detail the methods used to study a three-dimensional droplet on a rough surface. First we employ a homogenized approach that calculates the energy cost of having the droplet in two wetting states: Cassie-Baxter (CB) characterized by the suspension of the droplet trapping air inside the surface grooves, and the Wenzel state (W), where the liquid wets homogeneously the surface, both wetting states are schematized in Figure 1.5. By comparing their energy we define the stable thermodynamic state and then calculate the observables of interest, such as the contact angle and the droplet radius at the base. Then we use a Monte Carlo simulation of the cellular Potts model to further investigate two systems: a pure droplet of water and a droplet containing a mixture of water and oil. For the pure droplet we use a combination of restrained Monte Carlo with the string method to calculate the free energy. For the mixed droplet we extend the CPM to a four-state model to take into account the interaction between water and oil.

2.1 Wenzel and Cassie-Baxter models

As stated in the introduction, Robert Wenzel introduced a model to found that the contact angle from a flat surface differ from the *apparent* contact angle of a rough chemically homogeneous (noncomposite) surface by the factor of **r**, called *roughness*, and defined as the fraction between the real surface area and the projected surface area of a rough surface [2]. The relation between the angles can be written as

$$\cos\theta_{\mathrm{C}} = r\cos\theta_{\mathrm{Y}}. \tag{2.1}$$

This relation implies that changes in the surface roughness can increase the wetting behavior: a hydrophobic surface can become superhydrophobic and a hydrophilic surface can become superhydrophilic.

The Cassie-Baxter model assumes that air is trapped between the cavities of the surface [43]. Defining $\phi_{\mathrm{S}} = \mathrm{w}^2/\mathrm{d}^2$ as the fraction of solid surface area wet by the liquid (or pillar density), Cassie-Baxter relation is written as

$$\cos\theta_{\mathrm{C}} = \phi_{\mathrm{S}}\cos\theta_{\mathrm{Y}} - (1-\phi_{\mathrm{S}})\,. \tag{2.2}$$

Differently from Wenzel relation, Equation (2.2) allows a droplet of liquid with lower surface tension to have a repellent behavior. In other words, it is possible to have $\theta_{\mathrm{C}} > 90°$ even if $\theta_{\mathrm{Y}} < 90°$. Both relations are valid for the case where the droplet radius is much bigger than the size of the roughness. When the sizes are comparable, the energy from the interface liquid-gas (spherical cap of the droplet in contact with air) is comparable to the energy of the interface liquid-solid (fraction of the droplet that is wetting the surface) and therefore cannot be neglected, as discussed in the next section.

2.2 Homogenized approach: global energy model

Shahraz *et al.* proposed a model to predict the wetting state of a two-dimensional droplet on a rough surface [44]. Using energy minimization, it is possible to construct the wetting diagram as a function of the surface parameters. This model was then extended to account for a three-dimensional droplet by Fernandes *et al.* [45]. This method was also used to predict the global minimum of each wetting state for three types of surface, pillared, T-shaped and with double reentrance, while changing the surface tension to study different liquids [23].

We study a three-dimensional droplet with initial radius R_0 (volume $V_0 = 4\pi R_0^3/3$) placed on two surfaces, pillared (Figure 2.1-a) and porous (Figure 2.1-b). The parameters that characterize the surface are: width (w), interpillar distance (a) and height (h). We focus on the two wetting states defined previously, namely the CB (hydrophobic/oleophobic) and W (hydrophilic/oleophilic). To change the liquid type of the droplet the relevant parameters are the Young contact angle (θ_{Y}) and the surface tension between the gas G and liquid L (which can be water, w, or oil, o), σ_{GL}. For the droplet of water we use $\sigma_{\mathrm{GW}} = 72.8 \times 10^{-3}$ N/m and $\theta_{\mathrm{Y}} = 114°$, and for a droplet of n-Hexadecane oil we use $\sigma_{\mathrm{GO}} = 27.5 \times 10^{-3}$ N/m and $\theta_{\mathrm{Y}} = 53°$. The liquid-gas surface tension were taken from

[46]. For the solid-gas interaction we assume a surface composed by Polydimethylsiloxane (PMDS) with $\sigma_{\mathrm{SG}} = 25\times10^{-3}$ N/m [32]. We then calculate the solid-liquid surface tension for the water and oil using Young's equation $\sigma_{\mathrm{SL}} = \sigma_{\mathrm{SG}} - \sigma_{\mathrm{GL}}\cos(\theta_{\mathrm{Y}})$. This relation is geometrically obtained from Figure 1.1-a.

The total energy of each wetting state s (s=W or s=CB) is the cost to create an interface between the gas, liquid and solid phases to describe the state s. The global minimum approach calculates the difference between the interfacial energy of a droplet in the state s, E^s_{int}, minus the interfacial energy of the surface (without the droplet), E_{surf}:

$$\Delta E^s = E^s_{\mathrm{int}} - E_{\mathrm{surf}}. \tag{2.3}$$

The interfacial energy is given by the area of the interface A_{ij} times the surface tension σ_{ij}, where i, j are the pair of interfaces: gas-liquid, liquid-solid and gas-solid. The first term, E^s_{int}, is the energy to create the interface in the wetting state s, i.e., the contribution area times surface tension of each interface. The second term, E_{surf}, is the interaction between the surface and the gas (system before the droplet is placed on the solid). Equation 2.3 is a generalized equation to calculate the interfacial energy of creating a droplet in any wetting state over any type of surface.

For the case of a droplet on a Wenzel wetting state over a pillared surface, the contributions are the spherical cap of the droplet in contact with the gas (interaction liquid-gas), the liquid touching the solid (interaction liquid-solid) and the pillars touching the gas (interaction solid-gas). Equation 2.3 will be written as

$$\begin{aligned}\Delta E^{\mathrm{W}}_{\mathbf{pil}} &= \left(\sigma_{\mathrm{GL}} S^{\mathrm{W}}_{\mathrm{cap}} + \mathrm{N}^{\mathrm{W}}(\mathrm{d}^2 + 4\mathrm{hw})\sigma_{\mathrm{SL}}\right) - \left(\mathrm{N}^{\mathrm{W}}(\mathrm{d}^2 + 4\mathrm{hw})\sigma_{\mathrm{SG}}\right) \\ &= \mathrm{N}^{\mathrm{W}}\left[(\mathrm{d}^2 + 4\mathrm{hw})\left(\sigma_{\mathrm{SL}} - \sigma_{\mathrm{SG}}\right)\right] + \sigma_{\mathrm{GL}} S^{\mathrm{W}}_{\mathrm{cap}},\end{aligned} \tag{2.4}$$

The difference of the calculation for the CB state is that the droplet touches only the top of the pillars, creating two interfaces: the droplet touching the top area of the surface and the droplet in contact with the air between the pillars. For this wetting state, the energy is

$$\Delta E^{\mathrm{CB}}_{\mathbf{pil}} = \mathrm{N}^{\mathrm{CB}}\left[(\sigma_{\mathrm{SL}} - \sigma_{\mathrm{SG}})\mathrm{w}^2 + (\mathrm{d}^2 - \mathrm{w}^2)\sigma_{\mathrm{GL}}\right] + \sigma_{\mathrm{GL}} S^{\mathrm{CB}}_{\mathrm{cap}}, \tag{2.5}$$

where $\mathrm{d} = (\mathrm{w} + a)$, a being the distance between pillars and w the pillar width.

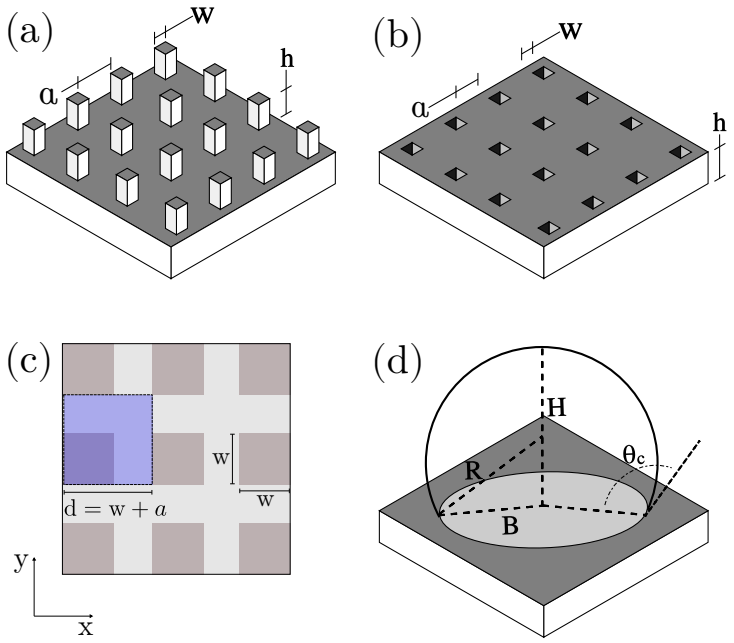

Figure 2.1: Definition of the geometric parameters of the substrates and the droplet. **(a)** Pillared surface with width (w), pillar distance (a), and height (h). **(b)** Porous surface with width (w), porous distance (a), and height (h). **(c)** Top view of the surface. Blue region delimits one cavity, used in the definition of the collective variables. **(d)** Geometric parameters of the droplet: spherical cap with radius R, base radius B and contact angle θ_{C}. Figure adapted from [22].

For the porous surface, the energy equations can be written as

$$\Delta E^{\mathrm{CB}}_{\mathbf{por}} = \mathrm{N}^{\mathrm{CB}}\left[(\mathrm{d}^2-\mathrm{w}^2)(\sigma_{\mathrm{SL}}-\sigma_{\mathrm{SG}})+\mathrm{w}^2\sigma_{\mathrm{GL}}\right]+\sigma_{\mathrm{GL}}S^{\mathrm{CB}}_{\mathrm{cap}}, \tag{2.6}$$

$$\Delta E^{\mathrm{W}}_{\mathbf{por}} = \mathrm{N}^{\mathrm{W}}\left[(\mathrm{d}^2-\mathrm{w}^2+4\mathrm{hw})(\sigma_{\mathrm{SL}}-\sigma_{\mathrm{SG}})+\mathrm{w}^2\sigma_{\mathrm{GL}}\right]+\sigma_{\mathrm{GL}}S^{\mathrm{W}}_{\mathrm{cap}}. \tag{2.7}$$

The total number of pillars (or pores) below the droplet is $N^s = \frac{\pi}{4}(2B^s/\mathrm{d})^2$, and $B^s = R^s\sin(\theta^s_{\mathrm{C}})$ is the base radius. The spherical cap area, which is in contact with the gas, is given by $S^s = 2\pi R^{s2}[1-\cos(\theta^s_{\mathrm{C}})]$. Superscript s denotes the state, s=W or s=CB.

In order to determinate the stable wetting state of a droplet with fixed volume on top of the pillared surface we apply the following minimization algorithm: **i)** fix surface parameters for pillars $(a, \mathrm{w}, \mathrm{h})$ and drop parameters (liquid type σ_{GL}, θ_{Y} and initial radius R_0). **ii)** by varying $\theta^s_c \in (0,\pi)$ we calculate the base radius B, spherical cap area S and number of pillars N. **iii)** using Equations (2.5) and (2.4) we compute ΔE^{CB} and ΔE^{W} for each value of θ^s_c. Then we search for the minimum value of those energies, $\Delta E^{\mathrm{CB}}_{\mathbf{min}}$ and $\Delta E^{\mathrm{W}}_{\mathbf{min}}$. **iv)** finally we compare the minimum values. The lowest energy obtained (either $\Delta E^{\mathrm{CB}}_{\mathrm{min}}$ or $\Delta E^{\mathrm{W}}_{\mathrm{min}}$) will correspond to the thermodynamic stable state. For the

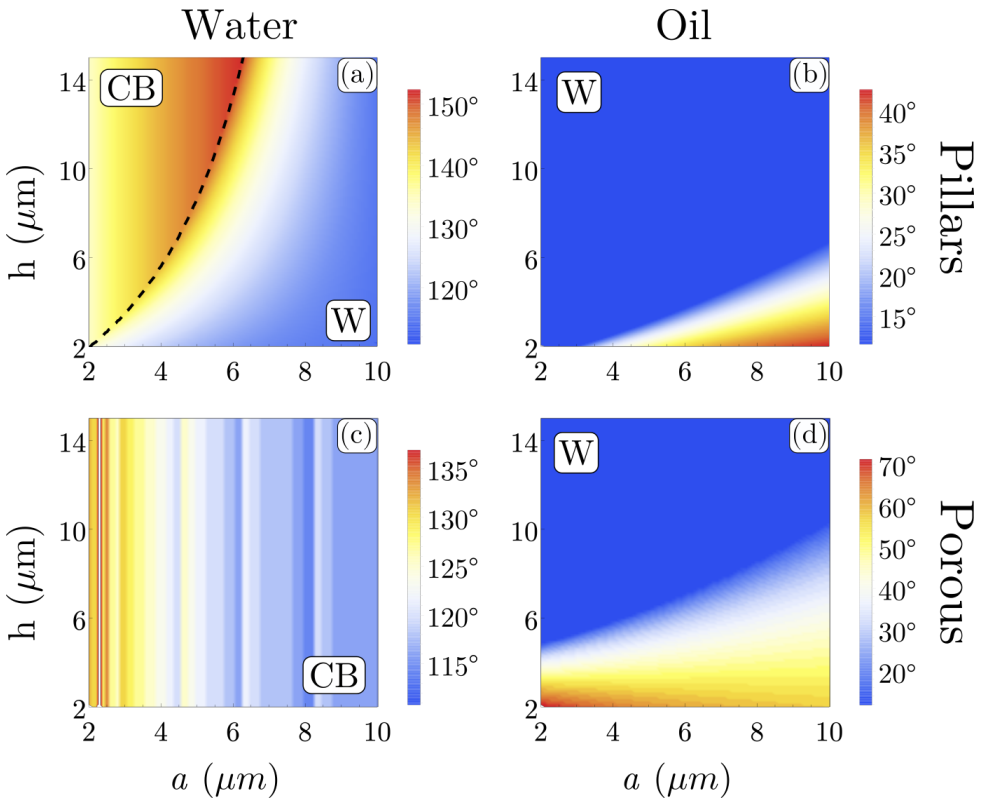

Figure 2.2: Theoretical wetting diagrams for **(a)** water droplet placed on a pillared surface, **(b)** oil droplet placed on a pillared surface, **(c)** water droplet placed on a porous surface and **(d)** oil droplet placed on a porous surface, as a function of two geometrical parameters of the surface: the height of the pillars (or pores) h, and the interpillar/interpourous distance a. Pillars width are kept constant w $= 5\mu$m. The dashed line in **(a)** represents the predicted thermodynamic transition between the Cassie-Baxter (CB) and (W) states. Colors indicate the droplet's contact angle, in degrees. Figure adapted from [22].

porous surface the only change in the minimization process is in step **iii)**, which we use Equations (2.6) and (2.7) to calculate $\Delta E^{\mathrm{CB}}_{\mathbf{por}}$ and $\Delta E^{\mathrm{W}}_{\mathbf{por}}$. A detailed example of this procedure is presented in Appendix A.

Figure 2.2 shows the contact angle (in degrees) as a function of the surface parameters (in micrometers). **(a)** is the result of a droplet of water on top of pillars. **(b)** is a droplet of oil on top of pillars. **(c)** the result for a droplet of water on top of a porous surface. **(d)** droplet of oil for porous surface. The only case in which we can see a clear transition between the states is for a droplet of water on top of pillars. For the three other cases the homogenized model predict only one wetting state: CB for a droplet of water on top of the porous surface and W state for the oil, independently of the surface.

The advantage of this simple method is that it allows us to study different surfaces and liquids. However, it limits us to only consider pure water or pure oil droplet,

disregarding the effects of water–oil interaction. Furthermore, for the particular case of pure water, this method also cannot predict metastable states, because it provides only the thermodynamically stable state. From experiments it is known that exists CB states that are metastable [5]. This indicates the existence of local energy minima and energy barriers, a feature which is not captured by this approach.

One explanation for the limitations of this method is the necessity to define the wetting states. For example, the theoretical CB state that we are proposing, as seen in Figure 1.5-a, has a flat interface liquid-gas above the droplet. From experiments (and later, using the MC simulation) we see that this does not correspond to the real case, where the droplet forms a meniscus due to the Laplace pressure. Another imposition in this model is that the liquid-gas interface between the pillars, Figure 1.5-b, for the Wenzel state is also considered flat. From the MC simulations we observe that this interface is in fact very rough. We will come back to this point in Chapter 3.

2.3 Monte Carlo simulation: pure water droplet

In this section we approach the problem described previously using Monte Carlo simulations of the cellular Potts model, technique first presented by Graner and Glazier in 1992 [47]. Mombach *et al.* were a pioneer in applying the CPM in the wetting field to study a two-dimensional droplet [48, 49]. In this work we use the three-dimensional extension of the model [45] to study the phenomenology of a droplet on a rough surface. The following section explains the CPM and how to identify metastable states. Then we use a restrained Monte Carlo combined with the string method to characterize the energy landscape of this system.

To simulate a droplet of pure water on a solid surface we use a three state system in a simple cubic lattice, with each site representing a different state: solid, liquid and gas. The Hamiltonian of this system is given by:

$$H_0 = \frac{1}{2}\sum_{\langle \mathrm{i,j}\rangle} E_{s_\mathrm{i},s_\mathrm{j}}\left(1-\delta_{s_\mathrm{i},s_\mathrm{j}}\right) + mg\sum_{\mathrm{i}} h_\mathrm{i}\ \delta_{s_\mathrm{i},1}, \tag{2.8}$$

where $s_\mathrm{i} \in \{0,1,2\}$ denotes the state of a given site i in the lattice: gas, liquid and solid, respectively. The first term on the right hand side describes the superficial interaction between the three states; note that only pair of spins with different states ($s_\mathrm{i} \neq s_\mathrm{j}$) have an energy contribution (we do not account for water-water interaction, for example). The

first sum runs over the third nearest neighbors of each site, which accounts for 26 total connections; E_{s_i,s_j} is the interaction strength between sites s_i and s_j, and δ_{s_i,s_j} is the Kronecker delta. The second term accounts for the gravitational energy, which acts only on sites in the liquid state, with $g = 9.81$ m/s^2. We find that the energy contribution of this term is usually much smaller than the superficial energy [45, 44, 50].

In our simulations the length scale is such that one lattice spacing corresponds to 1 μm and the surface tensions values are divided by 26, which is the number of neighbors that contributes to the first summation of our Hamiltonian. Therefore, the interfacial interaction energies $E_{s_i,s_j} = a_L\, \sigma_{s_i s_j}$, with $a_L = 1\mu\text{m}^2$, are given by $E_{0,1} = 2.70 \times 10^{-9}\,\mu$J, $E_{0,2} = 0.96 \times 10^{-9}\,\mu$J and $E_{1,2} = 1.93 \times 10^{-9}\,\mu$J. The mass in a unit cube is $m = 10^{-15}$kg.

To evolve the system we use the Metropolis-Hastings algorithm, which consists in changing the state of two random sites at the gas-liquid interface with an acceptance rate equal to $\min\{1, \exp[-\beta\Delta H]\}$, where $\beta = 1/T$ is the inverse of the effective temperature of the CPM, which acts as noise to allow a more effective exploration of the phase space. We set $T = 13$, which allows the system to fluctuate with an acceptance rate of approximately 9%. The attempted MC moves consist in swaps between liquid and gas sites, which guarantees that the volume of the droplet is constant throughout the simulation. The system can be initialized in two states: one configuration is a sphere of volume V_0 touching tangentially the surface, called CB^0 and shown in Figure 2.3-a. The second configuration is a hemisphere of same volume V_0 wetting the surface, called W^0 and shown in Figure 2.3-b.

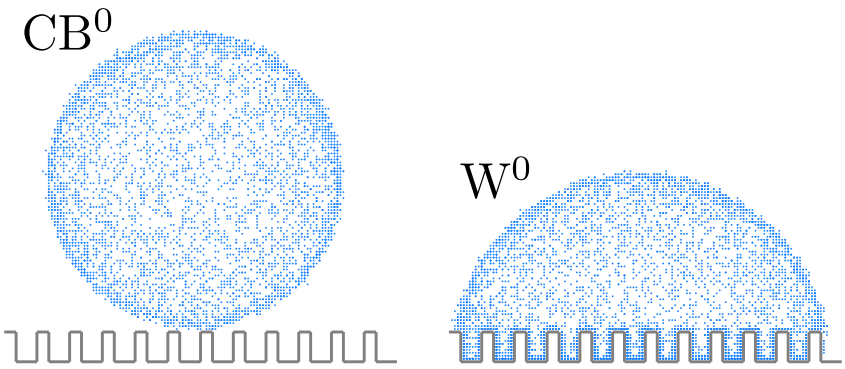

Figure 2.3: Initial wetting states for the Monte Carlo simulation: **(a)** sphere touching tangentially the surface, called CB^0, and **(b)** wetted state, called W^0. Figure taken from reference [45].

2.3.1 Metastable states

From experimental work, it is known that metastability is a phenomena present in this type of system [51, 52, 53, 54]. To identify and study this phenomena numerically, a previous work from our group [45] compared the contact angle obtained from the homogenized model, $\theta_{C,cont}$, and the contact angle obtained from the MC simulation, $\theta_{C,sim}$. In Figure 2.4 we show $\theta_{C,cont}$ in the x-axis and $\theta_{C,sim}$ in the y-axis. It was found cases were the system has low predicted contact angle but high simulated contact angle, meaning that these droplets, when initialized in the CB^0 state (Figure 2.3-a), are trapped in that metastable state due to an energy barrier that prevents from decaying to the global energy minimum. On the other hand, in pink circle we show the cases starting in the W^0 state (Figure 2.3-b), where there is a good agreement between the homogenized and numerical approaches. This figure is a reproduction of Figure 5-a from reference [45].

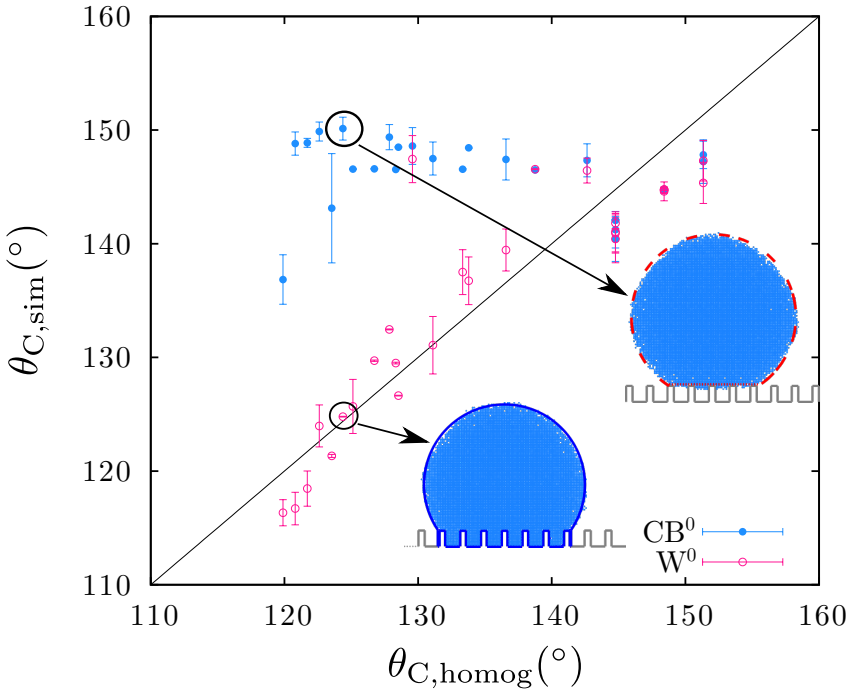

Figure 2.4: Scatter plot of contact angle between the homogenized approach and the MC simulations. Pink (blue) circles are simulations starting in the W^0 (CB^0) state.

The side view of the droplets shown inside this figure is an example of the comparison between the simulations and the homogenized approach. The droplet on top shows that when the system is initialized in the CB^0 state it remains in this metastable state with a good agreement with the predicted wetting state using Equation (2.5), red dashed line. The droplet below is for the system initialized in the W^0 state and the blue solid line is the predicted wetting state using Equation (2.4), which also show good agreement.

Figure 2.4 shows that the contact angle also depends on the initial wetting state, which indicates the presence of an energy barrier high enough that the droplet becomes trapped in the metastable state. Our goal now is to calculate the energy barrier that leads to these metastable phenomena and to systematically search for local energy minima. We will calculate the free energy profile of the system using a combination of the restrained MC simulations with the string method.

2.3.2 Restrained Monte Carlo

To calculate the free (Helmholtz) energy is of great interest because it allows us to quantify the energy barrier that leads to metastable states and to locate global and local energy minima. We will calculate the free energy difference as a function of the *collective variable*, a coordinate that can represent the different thermodynamic states [55]. In general, regions in the phase space around the energy minimum are well sampled, while regions of higher energy have a poor sampling. For rare events, those with an energy barrier significantly larger than $k_B T$, direct sampling is not computationally feasible. However, to obtain the energy profile $\Delta\mathcal{F}$, these high-energy regions must be sampled.

In order to sample the entire phase space we use the restrained Monte Carlo method. This technique consists on applying a bias term to the system in order to drive it into regions of higher energy to ensure efficient sampling. We create N_r replicas of the system and in each one we apply the bias with a different target value. The Hamiltonian is written as

$$H = H_0 + \frac{\kappa}{2} \sum_{l=1}^{l=N} \left(z_l - z_l^T \right)^2 , \tag{2.9}$$

where H_0 is the *unrestrained* system (no bias is being applied), described in Equation (2.8). The second term corresponds to the bias used to drive the system across metastabilities allowing to more freely explore phase space [56] as a function of general collective functions of the lattice sites z_l. Biasing is used because, in an *unrestrained* simulation ($\kappa = 0$), the droplet relax and remain trapped in the closest minimum energy state, as discussed in Section 2.3.1 and summarized in Figure 2.4.

The collective variables z_l that appear in Equation (2.9) should be chosen carefully [57] in order to correctly discriminate among relevant configurations of the system. In this work we shall identify z_l with the liquid-phase occupation of the l-th interpillar cavity. Each cavity (or groove), represented by the blue region in Figure 2.1-c, has an available volume given by $(\mathrm{d}^2 - \mathrm{w}^2)\mathrm{h}$. The usage of such discrete density indicators is customary when dealing with wettability problems [58]. Parameter κ is stiffness of the harmonic

constraint and z_l^T represents the target value for the collective variable. Note that, to simulate the CB state, we set $z_l^T \approx 0$, so there is no water in the cavities. Then, as we increase z_l^T, we reproduce different Wenzel states.

The choice of strength of the bias, κ, is a crucial step of this method. Values of κ too large and the sampling of the phase space becomes poor again. On the other side, if κ is too low then the initial wetting state will influence its final state and therefore the free energy calculation. The two criteria used to define the ideal κ are that the system should be driven to the target configuration, $z_l \to z_l^T$, and that the initial condition of the droplet does not influence over the final configuration. To test the values of κ we set z_l^T and perform the simulations with two different initial wetting states (with same volume V_0): CB^0 (Figure 2.3-a) and W^0 (Figure 2.3-b).

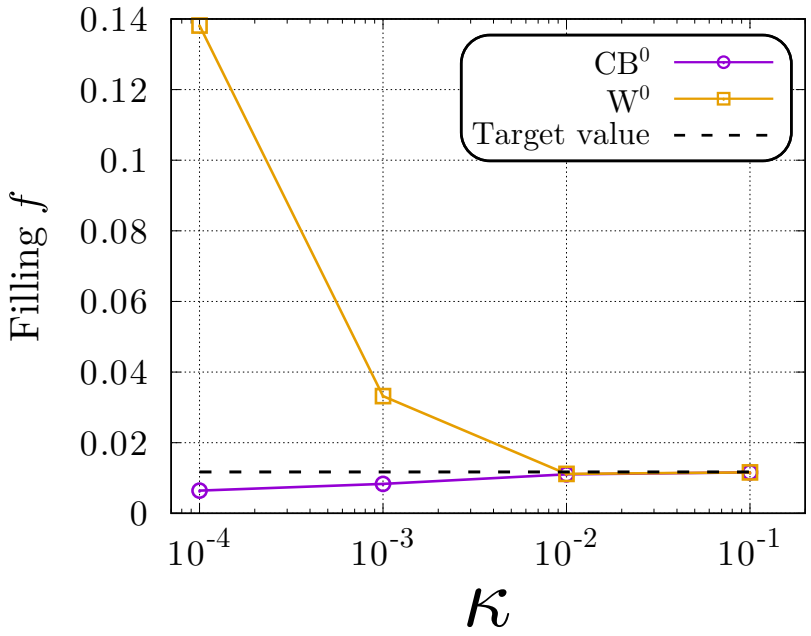

Figure 2.5: Filling f as a function of the coupling parameter κ. Dashed black line is the target value. The initial condition of the purple curve is a sphere touching the top of the pillar tangentially, Figure 2.3-a. Orange curve correspond to a simulation with a hemisphere wetting the surface as initial condition, Figure 2.3-b.

Figure 2.5 shows the filling f, defined as $f = \sum_{l=1}^{l=N} z_l^T/V_0$, as a function of κ. The filling can be interpreted as the fraction of water from the droplet that is wetting the surface. The black dashed line is the target value that we are imposing, the purple curve is the filling f of the simulation initialized in the CB^0 state and the orange curve is for f with simulation initialized in the W^0 state. As expected, when we increase κ the filling gets closer to its target value and the initial condition does not play a major role in the

final configuration. In addition, it is also favorable to have some fluctuation in the system. Therefore, we select $\kappa = 10^{-2}$, a value that drives the system to the target configuration while allowing thermal fluctuations.

2.3.3 String method

In order to attempt a simulation of the wetting of rough surfaces it is crucial to tackle the challenge associated with the presence of metastabilities. Previous methods to sample rough free energy landscapes required projecting to a low dimensional representation of the free energy as a function of a handful of parameters and reconstructing the full landscape as a function of such collective parameters [59, 60]. It is easy to understand how this task requires a computational effort which is exponential in the number of collective variables thus limiting the applicability of this class of methods typically to two/three variables. Such low dimensional representation of the energetic landscape often results in a poor description of the phenomena [57]. The (zero temperature) string method in collective variables was first introduced by Vanden-Eijnden and collaborators [56] and is a path method that requires only the computation of the *local* gradient of the free energy landscape at certain points along the path; its computational cost thus only grows linearly with the number of collective variables.

The string method allows for a fast and convenient identification of the minimum free energy path (MFEP) connecting two metastable regions of the rough landscape, along with providing a measure of the free energy along the path, without requiring to fully sample a high dimensional variable space. This is achieved by iteratively refining a discretized guess path (i.e., the string). The algorithm proceeds as follows:

1. We run N_r MC replicas, each biased to explore the vicinity of a point in the collective variable space $z^T_{l,i}$. Each replica, labeled by the index i, corresponds a string point in the collective variable space.

2. The N_r replicas are run for 10^5 MC moves allowing to sample the mean biasing forces $-\kappa\langle z_{l,i} - z^T_{l,i}\rangle$ which provide an estimate of the local free energy gradient at each string point.

3. The string is updated by a convenient gradient descent of the string points and reparametrized [61] so that one has a new set of $z^T_{l,i}$. The process is iterated from point **1**.

Refinement of the initial string guess is repeated until convergence is reached. In all runs convergence was obtained within 20 iterations. At convergence, the free energy is calculated using Thermodynamic Integration, technique detailed in the following section.

2.3.4 Thermodynamic Integration

Finally, having selected the optimal parameter κ and implemented the string method, we calculate the free energy difference $\Delta\mathcal{F}$ using the Thermodynamic Integration (TI) technique. From Maxwell's thermodynamic theory, we know that we can calculate the derivative of the free energy if we have access to some mechanical quantity. For example, the relation between pressure and $\mathcal{F}$, while maintaining volume V and number of particles N constant, is written as

$$\left(\frac{\partial\mathcal{F}}{\partial V}\right)_{T,N} = -P. \tag{2.10}$$

TI uses an analogy of Equation (2.10) to calculate $\partial\mathcal{F}$ and then we can obtain $\Delta\mathcal{F}$ by integrating, hence its name. This method is used because the absolute free energy and entropy cannot be measured in a MC simulation [62], since these quantities are directly related to the volume in the phase space, rather than an average of a function in the phase space.

Let's assume a system with potential energy $\mathcal{U}$ that depends linearly on a parameter λ. The partition function of this system can be written as

$$Q(\lambda) = \frac{1}{\Lambda^{3N}N!}\int dr^N \exp\left[-\beta\mathcal{U}(\lambda)\right], \tag{2.11}$$

and the associate free energy as

$$F(\lambda) = -\frac{1}{\beta}\ln\left[Q(\lambda)\right]. \tag{2.12}$$

We are interested in the derivative free energy is respect to the parameter λ, so

combining this with Equations (2.11) and (2.12) we obtain

$$\begin{aligned}
\frac{\partial \mathcal{F}}{\partial \lambda} &= -\frac{1}{\beta}\frac{\partial}{\partial \lambda}\ln\left[Q(\lambda)\right] = -\frac{1}{\beta Q(\lambda)}\frac{\partial Q(\lambda)}{\partial \lambda} \\
&= -\frac{\Lambda^{3N}N!}{\beta\int dr^N \exp\left[-\beta\mathcal{U}(\lambda)\right]}\cdot\frac{\partial}{\partial\lambda}\left(\frac{1}{\Lambda^{3N}N!}\int dr^N \exp\left[-\beta\mathcal{U}(\lambda)\right]\right) \\
&= -\frac{1}{\beta\int dr^N \exp\left[-\beta\mathcal{U}(\lambda)\right]}\int dr^N \frac{\partial}{\partial\lambda}\left(\exp\left[-\beta\mathcal{U}(\lambda)\right]\right) \\
&= -\frac{\int dr^N \left(\partial\mathcal{U}(\lambda)/\partial\lambda\right)\exp\left[-\beta\mathcal{U}(\lambda)\right]}{\int dr^N \exp\left[-\beta\mathcal{U}(\lambda)\right]} \\
&= \left\langle\frac{\partial\mathcal{U}(\lambda)}{\partial\lambda}\right\rangle, \qquad (2.13)
\end{aligned}$$

where $\langle\cdots\rangle$ denotes an ensemble average. Then, we can obtain the free energy difference $\Delta\mathcal{F}$ by integrating Equation (2.13):

$$\Delta\mathcal{F} = \int d\lambda \left\langle\frac{\partial\mathcal{U}(\lambda)}{\partial\lambda}\right\rangle. \qquad (2.14)$$

This is the formalism to a generic system. In the following we show how we calculate $\Delta\mathcal{F}$ for a system described by Equation (2.9). For clarity, the index will be suppressed. The Hamiltonian is

$$\begin{aligned}
H(s,z^T) &= \underbrace{\sum_{\langle \mathrm{i,j}\rangle} E_{s_\mathrm{i},s_\mathrm{j}}\left(1-\delta_{s_\mathrm{i},s_\mathrm{j}}\right)}_{H_0} + \underbrace{\frac{\kappa}{2}\sum_l \left(z_l - z_l^T\right)^2}_{g} \\
&= H_0(s) + g(z^T). \qquad (2.15)
\end{aligned}$$

The partition function of this system is written as

$$Q(s,z^T) = \sum_s \exp\left[-\beta H(s,z^T)\right]. \qquad (2.16)$$

The derivative of the free energy is respect to z^T is

$$\begin{aligned}\frac{\partial \mathcal{F}}{\partial z^T} &= -\frac{1}{\beta}\frac{\partial}{\partial z^T}\ln Q\left(s,z^T\right) = -\frac{1}{\beta Q\left(s,z^T\right)}\frac{\partial Q\left(s,z^T\right)}{\partial z^T} \\ &= -\frac{1}{\beta}\frac{1}{\sum_s \exp\left[-\beta H\left(s,z^T\right)\right]}\frac{\partial}{\partial z^T}\sum_s \exp\left[-\beta\left(H_0(s)+g\left(z^T\right)\right)\right] \\ &= \frac{1}{\sum_s \exp\left[-\beta H\left(s,z^T\right)\right]}\sum_s\left(\frac{\partial g\left(z^T\right)}{\partial z^T}\right)\exp\left[-\beta H\left(s,z^T\right)\right] \\ &= \left\langle\frac{\partial g\left(z^T\right)}{\partial z^T}\right\rangle. \end{aligned} \tag{2.17}$$

Finally, by integrating Equation (2.17), we have the free energy between two arbitrary points:

$$\Delta\mathcal{F}_j = \sum_{i=1}^{j}\sum_{l=1}^{l=N} -\kappa\langle z_{l,i} - z_{l,i}^T\rangle\Delta z_{l,i}^T\ , \tag{2.18}$$

with $\Delta\mathcal{F}_j$ the free energy at point $z_{l,j}^T$, the index l running over the N collective variables, i up to the current replica j, with $j \leq N_r - 1$, and $\Delta z_{l,i}^T = z_{l,i+1}^T - z_{l,i}^T$. The results shown are averages over the distinct realizations of the simulation and $\langle\dots\rangle$ represents the average over MC steps. In Chapter 3 we present $\Delta\mathcal{F}$ for a droplet of pure water on a pillared surface.

2.4 Monte Carlo simulation: mixed droplet

For the particular case of a mixed droplet composed of water and oil we expand the CPM to a four spin state, each one representing one of the components: gas, water, oil, or solid. The Hamiltonian is given by:

$$\begin{aligned} H &= \frac{1}{2}\sum_{<\mathrm{i,j}>} E_{s_\mathrm{i},s_\mathrm{j}}(1-\delta_{s_\mathrm{i},s_\mathrm{j}}) + \alpha_w\left(\sum_\mathrm{i}\delta_{s_\mathrm{i},1} - V_T^w\right)^2 \\ &+ \alpha_o\left(\sum_\mathrm{i}\delta_{s_\mathrm{i},2} - V_T^o\right)^2 + g\sum_\mathrm{i}(m_\mathrm{i}h_\mathrm{i}\delta_{s_i,1} + m_\mathrm{i}h_\mathrm{i}\delta_{s_\mathrm{i},2}), \end{aligned} \tag{2.19}$$

where the spin $s_i \in \{0,1,2,3\}$ represent gas, water, oil and solid states, respectively.

The first term in Equation (2.19) represents the energy related to the presence of interfaces between sites of different types. The second and third term accounts for the

volume of water (w) and oil (o), the summations are the water and oil volume, V_T^w and V_T^o are their target volumes, respectively, and the parameters α_w and α_o mimics the liquids compressibility. These terms are constraints in order to maintain the desired volume of water and oil constants throughout the simulations. The last term accounts for the gravitational energy, which has different strengths for water and oil. Here again the gravitational energy is much lower than the interfacial term.

Similar to the case of a pure water droplet, the interfacial energies are given by the value of surface tension between the phases. For the interaction water-oil the surface tension is $\sigma_{\mathrm{WO}} = 53.5 \times 10^{-3}$ N/m, the other values of surface tension are in Section 2.2. The interfacial energies are given by: $E_{0,1} = 2.70 \times 10^{-9}\mu$J, $E_{0,2} = 1.04 \times 10^{-9}\mu$J, $E_{0,3} = 0.96 \times 10^{-9}\mu$J, $E_{1,2} = 2.06 \times 10^{-9}\mu$J, $E_{1,3} = 1.93 \times 10^{-9}\mu$J and $E_{2,3} = 0.33 \times 10^{-9}\mu$J. The mass in a unit cube is $m^w = 10^{-15}$kg for water and $m^o = 0.77 \times 10^{-15}$kg for oil.

To evolve the system we use the Metropolis algorithm. A spin from the interface gas-water, gas-oil or water-oil is taken randomly and is attempted to flip it with probability $\min\{1, \exp(-\beta\Delta H)\}$. For the mixed droplet we use $T = 9$, which allows an acceptance rate of approximately 15% while keeping both water and oil in a liquid state, see Appendix B for more information about the value of T.

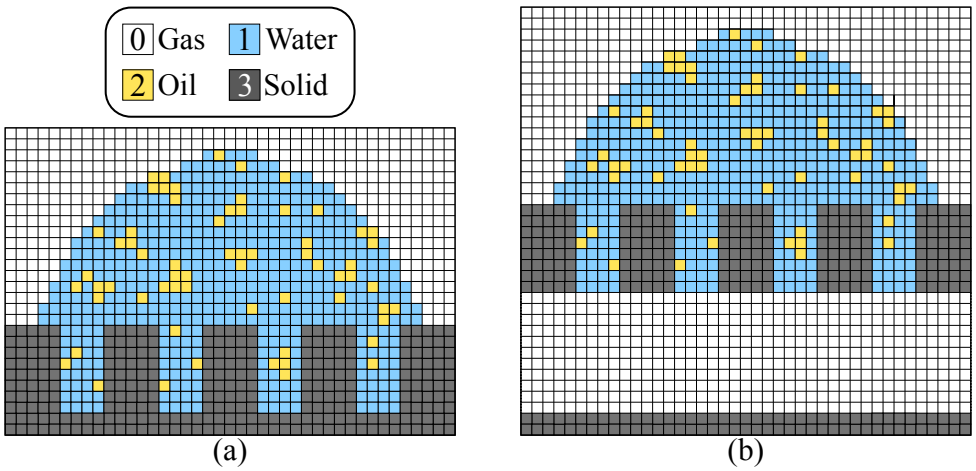

Figure 2.6: Visual scheme of the initial set up of the simulations for **(a)** the pillared surface and **(b)** the porous surface. Legend shows the label of the spins that represent each state.

For this particular case, we use W^0 as the initial wetting state used in the MC simulation, because of the metastability present when the system is initialized in the CB^0 state. The composition of the droplet is defined by the oil fraction f_o, thus, $V^o = f_o V^T$ is the oil volume and $V^w = (1 - f_o)\, V^T$ is the water volume. Oil and water sites are randomly distributed in the droplet. Two different substrates are studied as possible

oil-removing materials: pillared surface and porous surface. When the porous surface is used, a reservoir with volume $V_{\text{res}} > 3V_0$ is added to the bottom of the surface, as shown in Figure 2.6-b.

The next step in the simulation is adjusting the parameters α_w and α_o from Equation (2.19). The procedure is similar to the one used to select the parameter κ. To decide the values of the parameters we fix some values of α_w and then range α_o. In Figure 2.7 we show the volume of each component divided by its target value as a function of α_o with $\alpha_w = 0.01 \times 10^{-9} \mu\text{J}/(\mu\text{m})^6$. In this case we set $f_o = 0.50$, a droplet with equal parts of water and oil. As we can see from this figure, lower values α_o allow for fluctuations on the volume of both components. In this case we are studying a droplet with constant volume, so we will use $\alpha_w = \alpha_o = 0.01 \times 10^{-9} \mu\text{J}/(\mu\text{m})^6$.

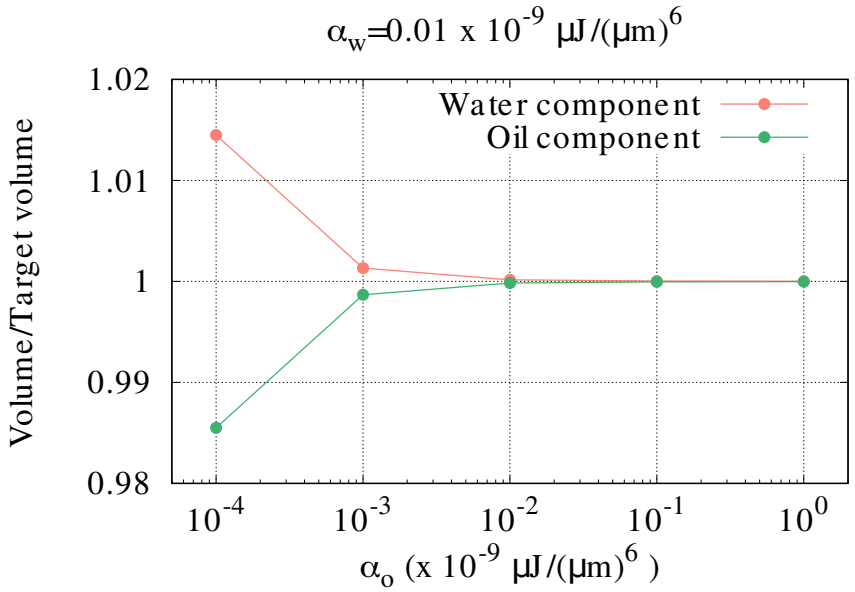

Figure 2.7: Green (coral) curve is the volume of the water (oil) component of the droplet divided by its target value for a drop with $f_0 = 0.50$. Figure from [22].

2.4.1 Efficiency

In order to evaluate the efficiency of the different substrates, we calculated the percentage of the initial oil/water volume that is between the pillars or inside pores, v_p^{L}, and, for the porous case, the percentage of the initial oil/water volume that is inside the reservoir, v_r^{L}. The superscription L refers to water, w, or oil, o. Here we call these quantities *percentage volumes* and they are calculated as follow:

$$v_p^{\text{L}} = V_p^{\text{L}}/V^{\text{L}}, \tag{2.20}$$

$$\upsilon_r^{\mathrm{L}} = V_r^{\mathrm{L}}/V^{\mathrm{L}}, \tag{2.21}$$

where V_p^{L} is the volume of the liquid (water or oil) between the pillar or inside the pores and V_r^{L} is the volume of the liquid inside the reservoir. V^{L} is the total volume of each liquid L. These percentage volumes allow us to define a liquid absorption capacity for the pillared and porous surface that measures how much of the initial liquid volume was absorbed by the substrate:

$$\epsilon_{\mathbf{pil}}^{\mathrm{L}} = \upsilon_p^{\mathrm{L}}, \tag{2.22}$$

$$\epsilon_{\mathbf{por}}^{\mathrm{L}} = \upsilon_p^{\mathrm{L}} + \upsilon_r^{\mathrm{L}}. \tag{2.23}$$

The ideal substrate for oil and water separation is, in our case, such that all the initial water volume remains above the surface and all the initial oil volume is adsorbed by the substrate. We then introduce a quantity to measure a separation efficiency that takes into account the capacity of a substrate to *simultaneously* retain the water and absorb the oil:

$$\xi_{\mathbf{S}} = \frac{\epsilon_{\mathbf{S}}^{o} + (1 - \epsilon_{\mathbf{S}}^{w})}{2}, \tag{2.24}$$

where the index S refers to the pillared or porous surface.

We also measured two efficiency that are commonly used in experiments. A surface with antagonistic wetting behavior is a good candidate to purify a mixed droplet. Gu *et al.* [63], and Singh *et al.* [64] engineered a substrate that displays a hydrophobic and oleophilic behavior. When a droplet containing water and diesel is placed over that surface and a reservoir is available, the diesel will pass through the surface into the reservoir while the water will stay on top of the substrate. In these articles, the authors calculate an efficiency that takes into account the amount of water that is not absorbed by the substrate. In our work, this efficiency can be calculated from the percentage of the water component that does not wet the surface (and reservoir):

$$\xi_{\mathbf{pil}}^{\mathbf{a}} = 1 - \upsilon_p^{w}, \tag{2.25}$$

$$\xi_{\mathbf{por}}^{\mathbf{a}} = 1 - \upsilon_p^{w} - \upsilon_r^{w}. \tag{2.26}$$

On the other hand, it is also possible to develop a surface that is hydrophilic and oleophobic [65, 66]. In this case, a mixed droplet that passes through this substrate will separate, since the oil will not wet the surface, while the water will be absorbed by it (and therefore can be collected after the purification). The efficiency measurement to describe this substrate is the capacity of the surface in rejecting the oil. It can be calculated by comparing the final concentration of oil in the remaining water above the surface, and the

initial oil concentration C_o. In our simulations, this efficiency will reflect the percentage of water that stays above the surface:

$$\xi^{\mathbf{r}}_{\mathbf{pil}} = 1 - \frac{1}{f_o}\left(\frac{V^o - V^o_p}{V^T - \left(V^w_p + V^o_p\right)}\right), \tag{2.27}$$

$$\xi^{\mathbf{r}}_{\mathbf{por}} = 1 - \frac{1}{f_o}\left[\frac{V^o - (V^o_p + V^o_r)}{V^T - [(V^w_p + V^w_r) + (V^o_p + V^o_r)]}\right]. \tag{2.28}$$

Chapter 3

Results and Discussion: metastability and predictability of the contact angle

In Chapter 2 we presented the numerical tools used to simulate a droplet on a rough surface. We concluded that the homogenized approach cannot reproduce the metastability of the CB state. This effect can, however, be reproduced employing Monte Carlo simulations of the cellular Potts model: a droplet initialized in one CB state will remain in it, even if this state is not a global energy minimum. The metastable regime is thus realized due to the presence of an energy barrier, which creates a local minimum. We then use a restrained Monte Carlo combined with the string method to force the system into visiting several wetting configurations and thus measure the free energy profile using thermodynamic integration.

In this chapter we present the numerical results obtained using the methods described previously. These results further clarify the occurrence of metastability for different surface parameters. Additionally, we quantify the energy barriers between the energy minima. Throughout this Chapter we will recurrently use the following variable: filling of the droplet, which is defined as the sum of the target filling of each cavity divided by the total volume of the droplet: $f = \sum_{l=1}^{N} z_l^T / V_0$. The energy unit, refereed as $e.u.$, is defined by $\sigma_{\mathrm{GL}} \cdot a_{\mathrm{L}}$, where a_{L} is the area of the lattice unit size. In order to convert the dimensionless units to physical ones, one can for instance assume the pixel area as $1\mu m^2$ and the energy for the gas-liquid interface of water, which yields $e.u. = 7 \times 10^{-14}$ J.

We consider three substrates with same pillar height h = 10 μm and width w = 5 μm

and different distances between pillars: substrate referred to as S_1 presents a low interpillar distance ($a = 5\mu$m), S_2 an intermediate value ($a = 8\,\mu$m), while S_3 has the largest interpillar distance ($a = 11\,\mu$m). Using the homogenized model we can predict the wetting state and contact angle for the three surfaces (shown in Figure 3.1). In Section 3.4 we compare the results from this homogenized model with the MC simulation. The volume of the spherical droplet is defined by imposing an initial radius of $R_0 = 50\,\mu$m (this radius corresponds to a droplet with volume of $\approx 0.5nl$).

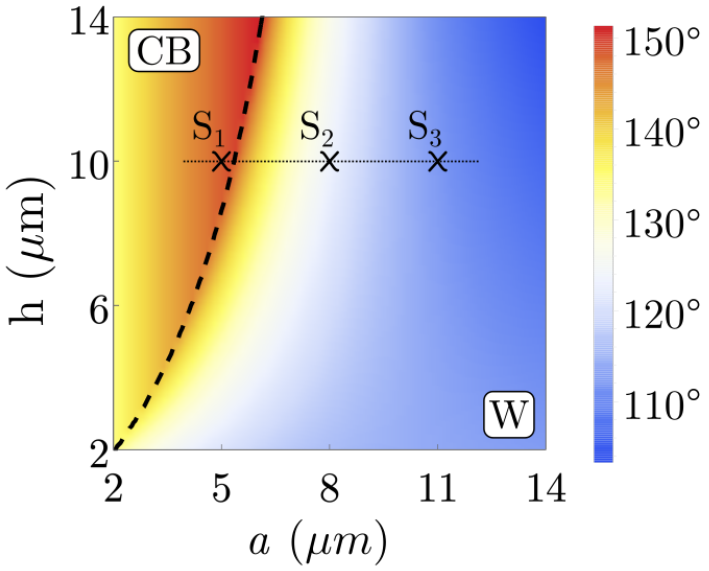

Figure 3.1: Theoretical wetting diagrams for a water droplet on a pillared surface as a function of h and a. Pillars width w $= 5\mu$m and droplet radius $R = 50\,\mu$m are kept constant. The dashed line in **(a)** represents the predicted thermodynamic transition between the Cassie-Baxter (CB) and Wenzel (W) states. Colors indicate the droplet contact angle, in degrees. The free energy will be calculated for surfaces with parameters given by S_1, S_2 and S_3. Figure adapted from [22].

We first show the rough free energy landscape connected with wetting of the three surfaces, characterizing the droplet configuration at the minima and maxima of the free energy. We then introduce a possible physical explanation of the roughness in the free energy and end this section discussing the connection between the free energy landscape and contact angle hysteresis.

3.1 Rough free energy of a hydrophobic pillared surface

Figure 3.2-a reports, for substrates S_1, S_2, and S_3, the free energy $\Delta\mathcal{F}$ of the drop as a function of the total filling f. The minima in the free energy correspond to stable (global) and metastable (local) states of the system. The free energy extrema are numerically identified from the data by deriving $\Delta\mathcal{F}$ in respect to f; minima are indicated in Figure 3.2-a as black circles, while maxima by red triangles. Empty symbol denotes minima that are so shallow that the system bypass the energy barrier. For the case of the closed symbol with seemingly shallow minima, we have verified that those are in fact minima in the free energy by performing several MC simulation to confirm that the system can indeed reside in such states.

Figure 3.2-b shows the fraction of water wetting the bottom area. The vertical dotted line in the figure is a guide to the eye and roughly separates two regimes: on the left, the liquid does not touch the bottom of the substrate, indicating that the corresponding configurations of the droplet are associated to the superhydrophobic CB state, while, on the right of the line, the liquid reaches the bottom of the substrate and the droplet configurations are associated with the wet W state(s). Importantly, the free energy landscape appears rough for all considered surfaces, with markedly different trends for the three interpillar distances: monotonically growing for S_1, almost at the CB-W coexistence, with additional high free energy minima, for S_2, and with a significant W basin with multiple local minima for S_3.

Each point on the free energy profiles corresponds to a droplet configuration, whose sequence thus defines a wetting path, see Figure 3.2-c; in particular, these paths represent the most probable way in which the transition from CB to one of the various W states (or vice versa) occurs. Other paths may exist connecting minima, especially in such complex landscape, see e.g. Ref. [67]. Figure 3.2-c presents a lateral view of the 3D droplet in correspondence of the minima and maxima of substrate S_3. Minimum I corresponds to the CB state, with air trapped between the pillars – this numbering is the same for the three substrates. As the droplet starts infiltrating the substrate, it touches the bottom for the first time at point II, where free energy increases to a maximum. A similar behaviour was also reported in molecular dynamics simulations [68, 69, 70, 71]. As the filling level increases, the free energy of the substrate presents several local minima which correspond to the progressive infiltration of liquid within the pillars: lateral views of the droplet in Figure 3.2-c clearly show full wetting of 3 lines of cavities at minimum III, 4 lines at V, 5 lines at VII.

For filling levels above 7 lines of cavities, the free energy does not present any other

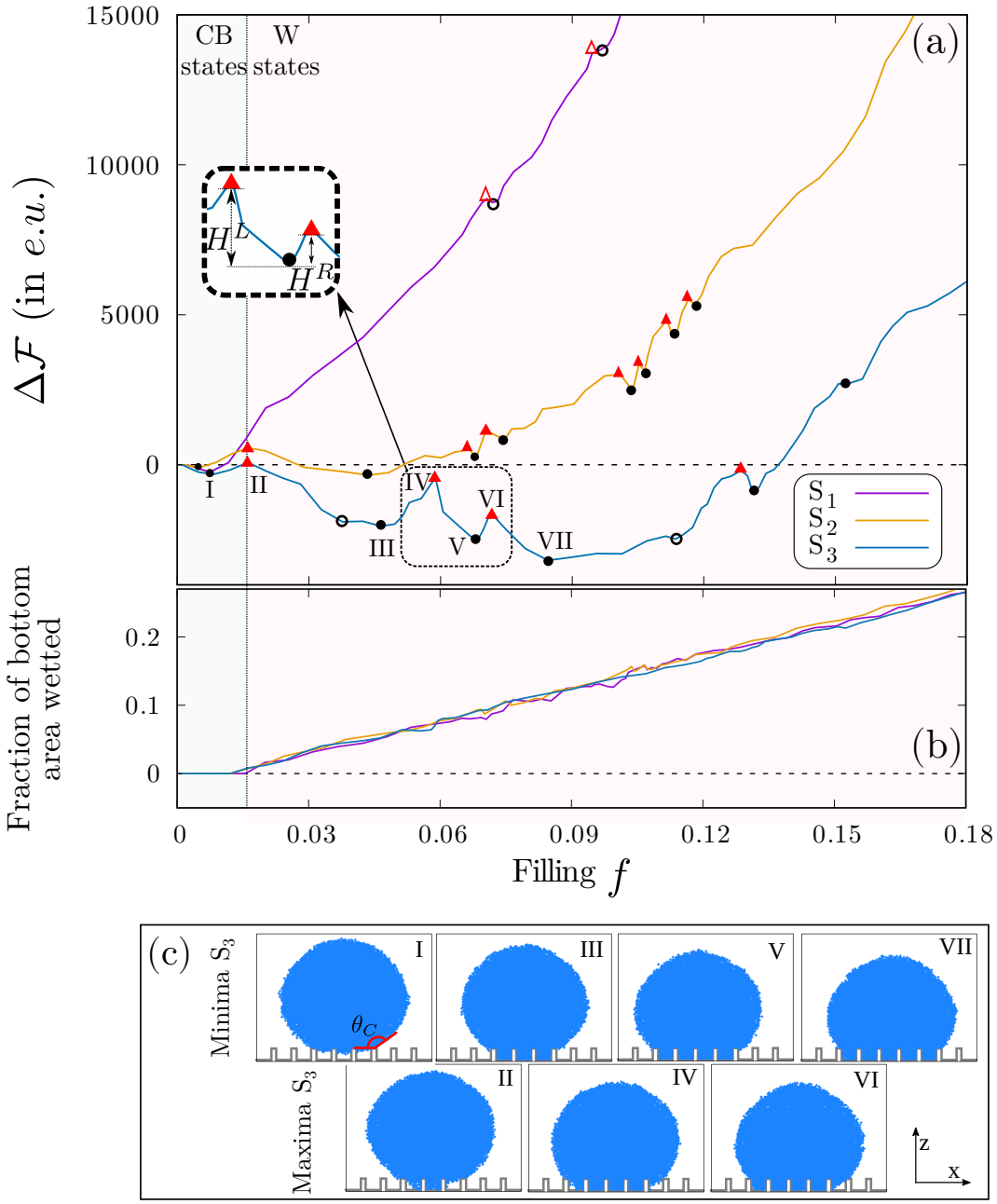

Figure 3.2: **(a)** Free energy profile as a function of the liquid filling the cavities for the three substrates. Minima are identified with black circles and maxima by red triangles; empty symbols denote very shallow minima (and related maxima) in which the system does not remain after standard MC minimisation. **(b)** Fraction of the bottom area of the substrate in contact with the liquid, normalized by the total substrate area. **(c)** Lateral view of the minima and maxima in the wetting of substrate S_3. The inset in **(a)** defines the left and right barriers, H^L and H^R, respectively.

minima. One possible explanation to this behavior is the limited volume of the droplet, which causes the cost to wet more rows of cavities to increase. We expect that, for bigger droplets, the free energy will present more minima related to the homogeneous wetting of the cavities.

The maxima separating the mentioned minima are found to be associated to an incomplete wetting of some of the cavities at the drop perimeter; we will further analyse their origin in Section 3.2. We note that the wetting of the substrate in 3D is a more complex problem than what can be inferred from a lateral view, which is however convenient to picture the main features of the process. In the Supporting Information section of the paper we make available videos in 2D and 3D of the droplet wetting the three substrates [21].

The inset of Figure 3.2-a defines the barrier H^L, which is the difference in $\Delta\mathcal{F}$ between a minimum and the consecutive maximum on its left and H^R, being the difference in $\Delta\mathcal{F}$ between a minimum and the first maximum on its right. Using these definitions, we found that the barrier H^R and H^L are typically of the same order of magnitude for substrate S_3, while for S_1 $H^L \ll H^R$. We will come back to this point later.

These observations raise several questions, which are addressed in the next section: why some substrates present global minima at the CB state and others in the W configuration? What is the physical origin and significance of the local minima and the intervening maxima?

3.2 Physical origin of the minima and maxima of the free energy

The wetting state corresponding to the global free energy minimum is different for the considered substrates and can be rationalized using the homogenized global energy model presented in Section 2.2.

The main difference between the model defined by Equation (2.4) and the Wenzel one (2.1) is that the former one considers a droplet of finite size, which means that the interface of the cap and the lower interface in contact with the substrate compete in the minimisation of the total free energy. We will return to this point in Section 3.4. Concerning the CB state, it is instead found that results are equivalent when one explicitly considers the cap as in Equation (2.5).

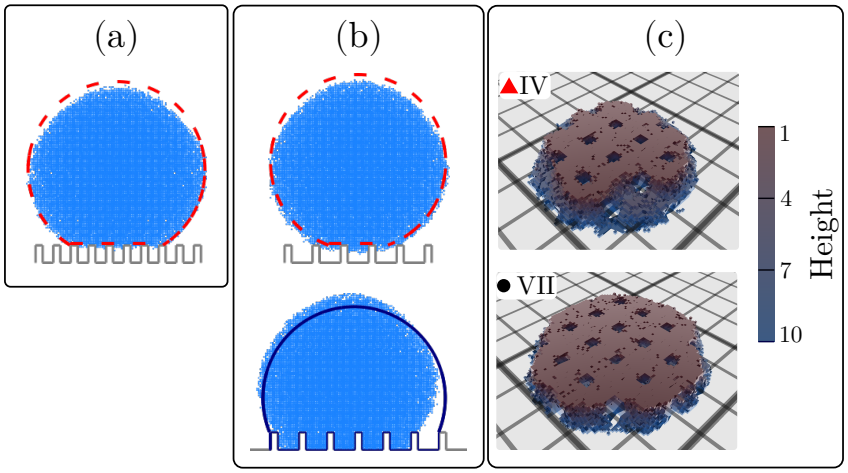

Figure 3.3: **(a)** Side view of configuration at the minimum of $\Delta\mathcal{F}$ for surface S_1 in blue. Red dashed line is the numerical solution of the homogenized model for the CB state, Equation (2.5). **(b)** Top: side view of a droplet on surface S_3 at the local minimum of $\Delta\mathcal{F}$ (point I in Figure 3.2) and the solution of Equation (2.5). Bottom: global minimum of $\Delta\mathcal{F}$ in the W state (point VII in Figure 3.2). The blue solid line is the numerical solution of the model in Equation (2.4) for the W state. **(c)** View from below of the 3D configuration of the droplet placed on S_3 at two filling levels: point IV in Figure 3.2-a (maximum) and point VII (global minimum); colors correspond to the height of liquid in each lattice site.

Figures 3.3-a,b shows the lateral view of the droplet obtained from the MC simulation for the surface S_1 and S_3, respectively. For surface S_1, $\Delta\mathcal{F}$ presents only one minimum for which the simulated configuration is shown in blue together with the minimum of the solution of Equation (2.5), in red. $\Delta\mathcal{F}$ of surface S_3 has multiple minima and two of them are represented in Figure 3.3-b: the local minimum at the CB state, shown on top with the solution of Equation (2.5), and the global W minimum reported in the bottom panel, in which is compared with the solution of Equation (2.4). Results are in good agreement for the CB state, both concerning the contact angle and the number of intruded cavities. On the other hand, contact angles are not in perfect agreement for the W state, due to the local pinning at pillars, which is not captured in Equation (2.4). On the other hand, the model predicts correctly that W is the global free energy minimum and the free energy values are in reasonable accord.

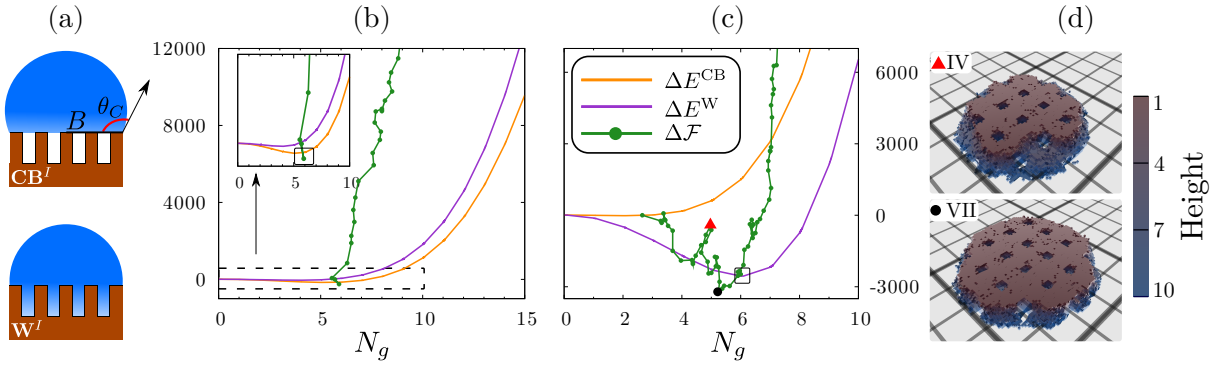

Figure 3.4: Homogenized model *vs* $\Delta\mathcal{F}$. **(a)** Two types of configurations for the droplet considered in the homogenized model, CB and W. **(b)** Numerical solution of Equations 2.5 and 2.4 compared to $\Delta\mathcal{F}$ for S_1 as a function of the *linear* row of cavities wetted. The inset in this figure is a zoom around the minimum value. **(c)** Same as in (b) for S_3. Energies are displaced by the same fixed value in y-axis to be able to compare with the variation of the free energy. Global minimum of the homogenized model is indicated by the open square. **(d)** Images of the 3D configurations of the droplet placed on S_3 for two values of fillings: in the maximum indicated by the red triangle in **(c)** and corresponding to the point IV in Figure 3.2-a and in the local minimum indicated by the black circle and corresponding to the point VII in Figure 3.2-a. This is a view from below and colors correspond to the filling of liquid in each pixel.

In Figure 3.4 we show a comparison between the numerical simulation and the homogenized model. A sketch of CB and W is shown Figure 3.4-a. The green curve in panel **(b)** (for S_1) and **(c)** (for S_3) is the free energy from the MC simulation, $\Delta\mathcal{F}$, as a function of the *linear* cavities wetted. In orange we plot the the energy from Equation (2.5) and in purple is the energy from Equation (2.4). In panel **(d)** we present the 3D visualization for the red triangle (maximum in $\Delta\mathcal{F}$) and black circle (global minimum in $\Delta\mathcal{F}$) highlighted in panel **c**. This is a view from below and the colors correspond to a pixel being filled by water or not. In this visualization we can see clearly the roughness of the area liquid-vapor, which is a key point for understanding the local minima discussed in the main text.

Figures 3.4-b,c show that there is a reasonable agreement between the homogenized model and the simulation. For S_1 it is observed that $\Delta E^{CB} < \Delta E^{W}$, which means that the model predicts the droplet in the CB state. From $\Delta\mathcal{F}$ we see that the global minimum agrees with the prediction, the droplet is on the CB state on top of a similar value of pillars. For S_3 the picture is much more complex. The model predicts a drop on the Wenzel state wetting, although it cannot predict local minima, only the global one. On the other hand $\Delta\mathcal{F}$ does show many minima and, although they are not predicted, we observe that they are well aligned in the purple curve. For this surface the global minimum

predicted and the one calculated does not agree quantitatively.

Besides the fair agreement at the global minimum, the main difference between the two approaches is that the simulated free energy profile presents several local minima which are not accounted for in any of the homogenized models. This difference is particularly important for the W state, in which pinning of the three-phase contact line plays a major role. Indeed, an important simplification introduced in the model (2.4) is that the W state is achieved by *homogeneous* wetting: below the droplet base, there is a perfect cylinder filling the cavities; individual wetting of pillars is thus disregarded; the cost to create the interface between the liquid and air is also neglected in the model. However, simulations show that the infiltration of the substrate is not homogeneous, that pinning at individual pillars may occur, and that the interface between the liquid and the gas below the droplet is quite rough, as exemplified in Figure 3.3-c for one minimum and one maximum: the configurations are particularly far from being a cylinder when $\Delta\mathcal{F}$ is at a maximum.

The nontrivial shape of the droplet in contact with the surface drove us to investigate the contribution to the free energy of each interface. We propose a putative free energy defined as: $\Omega = \Delta P\, V_0 + \sigma_{\mathrm{GL}} A_{\mathrm{GL}} + \sigma_{\mathrm{SL}} A_{\mathrm{LS}} + \sigma_{\mathrm{SG}} A_{\mathrm{SG}}$, where ΔP can be interpreted as the Laplace Pressure, $\Delta P = -\alpha\sigma_{\mathrm{GL}}$ with α being the mean curvature of the drop and A_{ij} are the interfaces between two different phases ij (solid, liquid, and gas). We then use the Young equation $\sigma_{\mathrm{SG}} = \sigma_{\mathrm{SL}} + \sigma_{\mathrm{GL}} \cos\theta_{\mathrm{Y}}$ to rearrange the terms and note that the total area of the substrate $A_{\mathrm{tot}} = A_{\mathrm{LS}} + A_{\mathrm{SG}}$ is constant. The contribution of liquid-gas surface area A_{GL} is split in two parts, one corresponding to the surface of the spherical cap $A^{\mathrm{C}}_{\mathrm{GL}}$, and other to the part below the droplet, $A^{\mathrm{B}}_{\mathrm{GL}}$. We can then write the difference in free energy with respect to the reference one $\Omega_{\mathrm{ref}} = \sigma_{\mathrm{SG}} A_{\mathrm{tot}}$:

$$\Delta\Omega = \sigma_{\mathrm{GL}} \left(A^{\mathrm{C}}_{\mathrm{GL}} - \alpha V_0 \; + \; A^{\mathrm{B}}_{\mathrm{GL}} - A_{\mathrm{LS}} \cos\theta_{\mathrm{Y}} \right). \tag{3.1}$$

Interestingly, the surface tension σ_{GL} factorises and only geometrical quantities appear in the parenthesis on the right hand side, together with the Young contact angle θ_{Y}.

Figure 3.5-a compares, for surface S_3, the free energy $\Delta\mathcal{F}$ obtained in the MC simulations via Equation (2.18) with the putative free energy $\Delta\Omega$ always computed from MC simulations but by measuring the geometrical quantities in Equation (3.1). In particular, the surface areas A_{ij} and the mean curvature $\alpha = 2/R$ are measured from droplet configurations along the converged string. Note that the Monte Carlo simulations takes into account the curvature of the droplet without having to add this contribution explicitly. Since the free energy $\Delta\mathcal{F}$ is computed by integration, it is known up to a

constant and thus can be freely displaced along the y-axis.

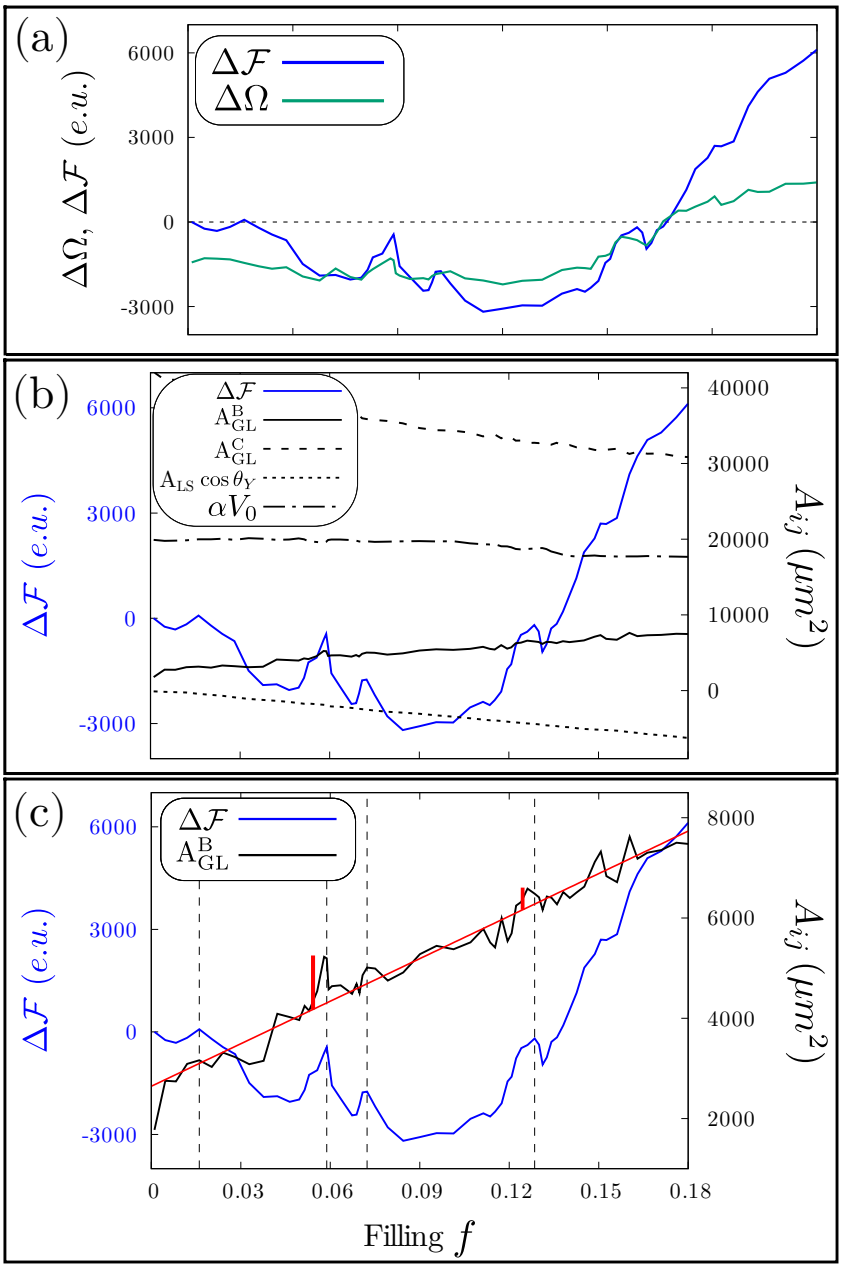

Figure 3.5: $\Delta\mathcal{F}$, $\Delta\Omega$ and areas as a function of f for S_3. **(a)** Comparison of $\Delta\mathcal{F}$ and $\Delta\Omega$. **(b)** The free energy $\Delta\mathcal{F}$ is shown in blue (left axis) and the components of Equation (3.1) are shown in black (right axis): solid line is A^{B}_{GL}, dashed line is A^{C}_{GL}, dotted line is $A_{LS}\cos\theta_Y$, and dot-dashed line is αV_0. **(c)** Free energy in blue and A^{B}_{GL} in black. The red curve is a linear fit of A^{B}_{GL} and the red vertical lines indicate the area variations discussed in the text. Dashed lines denote the maxima of $\Delta\mathcal{F}$. Young contact angle is fixed at $\theta_Y = 114°$, so $\cos\theta_Y \approx -0.4$.

Using the same value for σ_{GL} as the simulation, Figure 3.5-a shows $\Delta\mathcal{F}$ and $\Delta\Omega$ for surface S_3. The two quantities show similar trends and are in semi-quantitative agreement

for all three substrates analysed in this work. Interestingly, the ruggedness observed in $\Delta\mathcal{F}$ is also present in $\Delta\Omega$. Additionally, line tension (the linear contribution from the water-gas interface), which is not accounted for in Equation (3.1), could in principle play a role; its value, however, is not known for CPM. Physically, one would expect line tension to be of the order of tens of piconewtons for water in contact with hydrophobic silica [72, 58]; such figure would account for noticeable line effects only for nanometer-sized pillars [73, 74].

In Figure 3.5-b, we show the free energy profile, in blue, and all areas component of Equation 3.1 as a function of f: full line is the area of the gas-liquid interface below the droplet $A^{\mathrm{B}}_{\mathrm{GL}}$, dashed line is the gas-liquid interface area of the spherical cap $A^{\mathrm{C}}_{\mathrm{GL}}$, dotted line is the liquid-solid component $A_{\mathrm{LS}}\cos\theta_{\mathrm{Y}}$, and dotted-dashed line is the Laplace pressure term αV_0. Note the different scales and units for areas (right axis) and $\Delta\mathcal{F}$ (left axis). All components, except $A^{\mathrm{B}}_{\mathrm{GL}}$, have a smooth dependence with f, and therefore is a good candidate to explain the roughness of the free energy connected to wetting. In Figure 3.5-c we show the free energy in blue and the component $A^{\mathrm{B}}_{\mathrm{GL}}$ in black. Vertical dashed lines correspond to maxima of $\Delta\mathcal{F}$. We observe variations in the curve of $A^{\mathrm{B}}_{\mathrm{GL}}$ that are indicated by vertical red lines. The typical size of these variations is $\Delta A^{\mathrm{B}}_{\mathrm{GL}} \approx 1000\,\mu m^2$. In terms of dimensionless energy, this corresponds to $\Delta A^{\mathrm{B}}_{\mathrm{GL}}\sigma_{\mathrm{GL}} \approx 1000$. This energy variation is comparable to the free energy barrier for S_3, $\Delta A^{\mathrm{B}}_{\mathrm{GL}}\sigma_{\mathrm{GL}} \approx H^R$, which suggests that the term relative to the interface between liquid and gas below the droplet plays an important role in generating local minima in the free energy.

In the previous section, we mentioned that local minima of $\Delta\mathcal{F}$ correspond to pinning of the drop at the pillars edges, which gives rise to several possible minimal configurations characterized by different numbers of pillars. To connect this picture with the observation that variations of $A^{\mathrm{B}}_{\mathrm{GL}}$ correlate with variations of $\Delta\mathcal{F}$, we suppose that the wet domain below the droplet can be approximated by a cylinder of height h and increasing radius B, such that $A^{\mathrm{B}}_{\mathrm{GL}} = 2\pi hB$. This approximation does not take into account the roughness of $A^{\mathrm{B}}_{\mathrm{GL}}$ shown in Figure 3.3-c, but is reasonable in the case of minima. From the volume differences between neighboring minima in Figure 3.5 we can thus compute the jump in droplet radius ΔB in the cylindrical approximation, $\Delta B \approx \Delta A^{\mathrm{B}}_{\mathrm{GL}}/(2\pi h) \approx 16\,\mu m$. The estimated value of ΔB corresponds to the typical size of a cavity $\mathrm{d} = \mathrm{w} + a$, which is plausible and supports the idea that local minima correspond to jumps of the droplet front across discrete numbers of pillars.

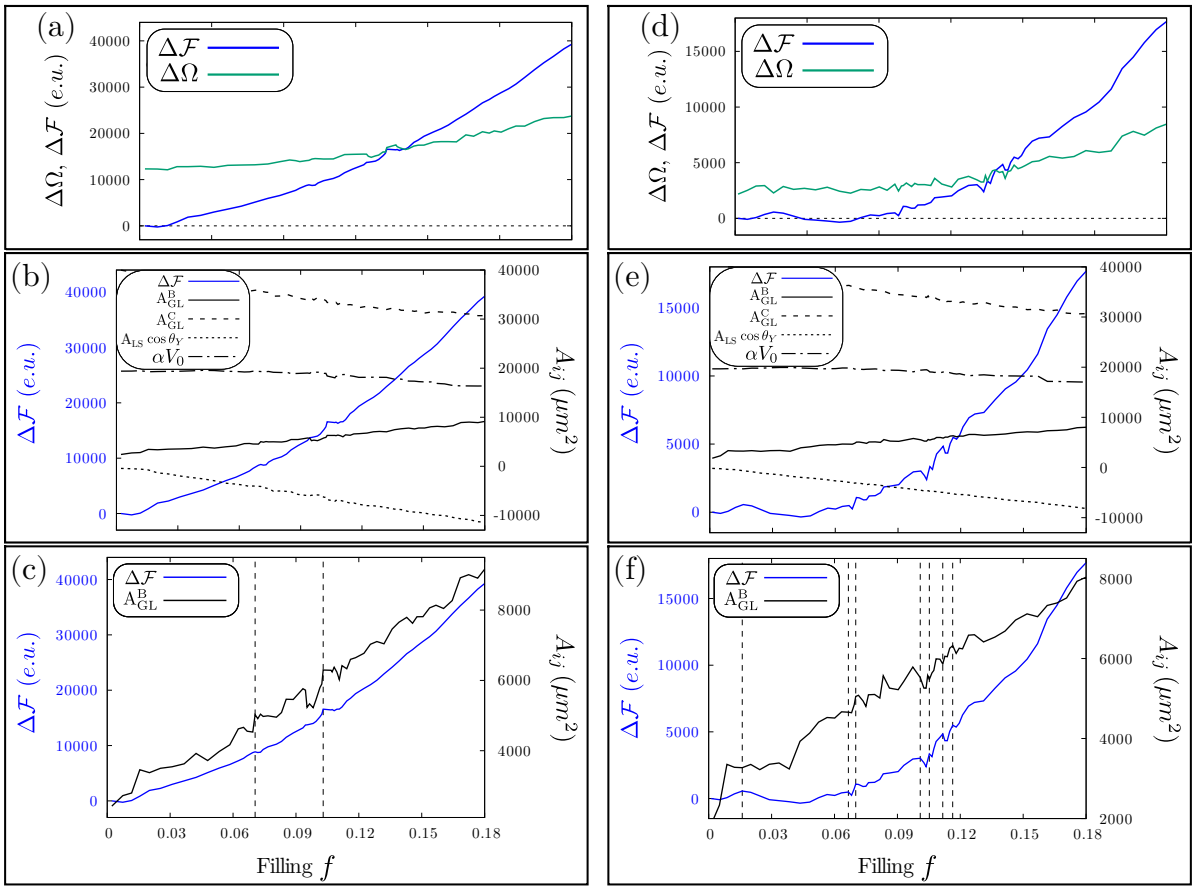

Figure 3.6: $\Delta\mathcal{F}$, $\Delta\Omega$ and areas as a function of f for S_1 on the left and S_2 on the right. Comparison of $\Delta\mathcal{F}$ and $\Delta\Omega$ for **(a)** S_1 and **(b)** S_2. The free energy $\Delta\mathcal{F}$ is shown in blue (left axis) and the components of Equation (3.1) are shown in black (right axis): solid line is A^{B}_{GL}, dashed line is A^{C}_{GL}, dotted line is $A_{LS}\cos\theta_Y$, and dot-dashed line is $-\alpha V_0$. **(c)** Free energy in blue and A^{B}_{GL} in black. Dashed lines denote the maxima of $\Delta\mathcal{F}$.

In Figure 3.6 we show the same comparison between $\Delta\mathcal{F}$ and $\Delta\Omega$ and its components, for surface S_1 on the left and S_2 on the right. In the particular case of S_1, abrupt variations of A^{B}_{GL} are not sufficient to generate local minima, due to the steep slope of $\Delta\mathcal{F}$ vs f. Surface S_2 has a behavior similar to S_3, in which the fluctuations of the area A^{B}_{GL} are high enough to be a good source of explanation on the origins of the local minima.

To summarize, we propose that the global minimum of the free energy corresponds to configurations that minimize the total interfacial energy for a droplet of fixed volume. Local minima, instead, occur in correspondence of abrupt variations of the liquid-vapor interface below the droplet connected with the overcoming of individual pillars.

3.3 Minima of the free energy and contact angle hysteresis

We now evaluate the free energy barrier sizes that separate the local minima and the consequences on the metastability of the substrates. From Figure 3.2-a, one measures for S_1 typically $H^R \in (3000, 9000)$ and $H^L \in (0, 100)$ showing that, even when the system is initialized in the W^0 state, it rapidly evolves towards the CB minimum. For substrate S_3 both barriers vary typically in the range $H^R \approx H^L \in (370, 3700)$, which in physical units are between 9×10^{-12}J and 9×10^{-11}J. This is much higher than the thermal energy $k_B T \approx 4.1 \times 10^{-21}$ J at ambient temperature: thermal fluctuations are not sufficient to drive the system from one minimum to the other. Only other larger sources of energy can move the drop away from local minima, e.g., mechanical vibrations.

When the system is prepared with some generic initial condition, it will fall in the closest minimum and remain trapped there; this was verified by running unrestrained MC simulations from several points along the curves in Figure 3.2-a. Only for the S_1 the system always returned to the superhydrophobic CB state, even though two shallow minima were identified numerically; this can possibly be either due to the numerical accuracy of the free energy profiles or to the size of the barriers, which is so low that the fluctuation imposed by the effective temperature of the Monte Carlo simulations are enough to bypass them. In other words, the free energy profiles in Figure 3.2 help understanding the origin of contact angle hysteresis in contact angle measurements, which can be rationalised in terms of a rough free energy landscape with multiple minima, separated by large free energy barriers. Furthermore, the importance of the initial conditions becomes apparent, which are determined by the preparation phase and drop deposition in a sessile drop experiment. As an example of an actual experiment, the drop can be placed on the surface at different initial wetting states, which can be achieved by depositing it carefully or letting the droplet fall from different heights [5]. If the free energy of the substrate presents multiple minima, the final wetting state of the droplet (and consequently its contact angle) would be different; this indeed is observed in experiments [5] which indicates the presence of hysteresis in the contact angle.

Finally, the profiles account for the superhydrophobic properties of the CB state, which are connected to the existence of a single minimum, i.e., with low hysteresis. On the other hand, the presence of multiple W minima explains why CAH is so pronounced in this wetting state and its stickiness [5, 52, 54]. Figure 3.7 shows the apparent contact angle θ_C of the droplet measured in MC simulations together with $\Delta\mathcal{F}$ for substrate S_3. The fact that there is a basin of Wenzel states and that each minimum has a different contact angle allows us to define the contact angle hysteresis θ_H related to the wet W

state as the difference in θ_C of the configuration associated to the first and the last local Wenzel minimum of $\Delta\mathcal{F}$, see Figure 3.7. Table 3.1 summarizes the values θ_H for the three substrates together with their roughness ratio r. We measured an increase of θ_H when r decreases, which is in line to what was previously observed [75]. We also observe that, when the roughness increases, the minimum corresponding to the CB state becomes more prominent, which is consistent with recent simulations of a droplet of gallium on a pillared surface [76].

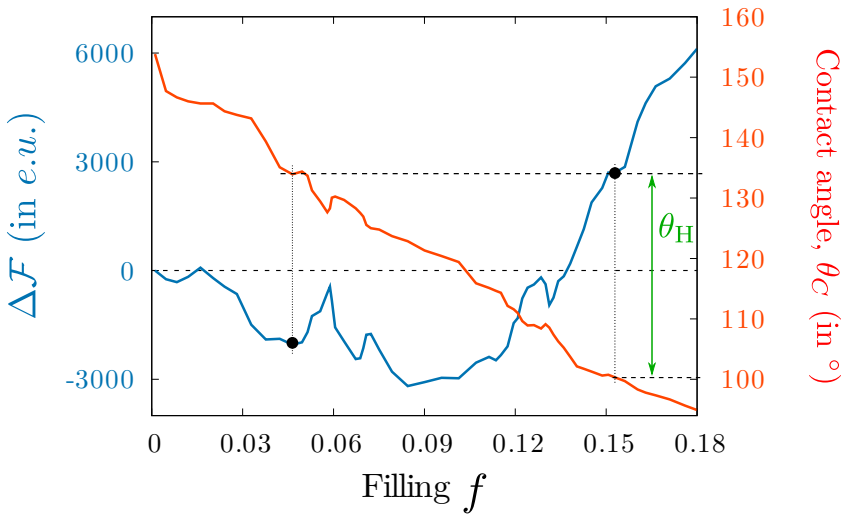

Figure 3.7: Wetting free energy and apparent contact angles as a function of liquid filling for substrate S_3. The scale on the left corresponds to $\Delta\mathcal{F}$ and, on the right, to θ_C. The difference between the θ_C associated to the first and last local minimum (indicated as black circles) is defined as the θ_H.

Substrate	roughness ratio, r	θ_H, (in °)
S_1	3	0
S_2	2.2	24°
S_3	1.8	36°

Table 3.1: Contact angle hysteresis θ_H and roughness ratio r for the considered substrates.

3.4 Discussion: modeling rough wetting

We have identified by free energy simulations that some pillared substrates present several local minima separated by high barriers, while others present only one minimum. Incidentally, for tall/tightly packed pillars only the superhydrophobic CB state is possible, while for more sparse pillars multiple local wet minima arise. The latter surfaces thus display a

behaviour which is strongly dependent on the initial conditions: if a droplet is deposited on a substrate at a random configuration or with a different experimental procedure, it would accommodate in a wetting state correspondent to the closest minimum which can be either superhydrophobic or sticky.

The present findings also imply that theories that predict a single W state cannot be complete [77]. The goal of this section is to critically discuss the predictions of representative theories based on the homogenization of surface energies and contrast them with the results of our simulations, which here play the role of an *in silico* experiment.

We measured all apparent contact angles θ_C of the droplet in configurations correspondent to physical minima identified in our simulations for the three substrates and compared them with theoretical models, see Figure 3.8. Squares corresponds to the superhydrophobic CB minimum and circles to wet W states. Lines are solutions of the classical Wenzel and Cassie-Baxter models, whose apparent contact angles are given by Equations (2.1) and (2.2), respectively.

For the case where the global minimum is CB, which happens for substrate S_1, Figure 3.8 shows that the prediction of the Cassie-Baxter model is almost quantitative. The CB model also has a reasonable agreement with simulated θ_C in cases where it is only a local minimum, which happens for substrates S_2 and S_3. The agreement with CB model deteriorates as the pillar distance increases, which can be explained by the increasing curvature of the menisci suspended among pillars, not accounted for in the classical CB model.

In principle, no direct comparison can be made between the W model and the MC results, mainly because the model predicts only one state, while simulations demonstrate the existence of multiple wet states. However, a fair comparison can be made considering only the global minimum, which is compatible with the minimization procedure used in the homogenized models. It is seen that the W model prediction is far from the measured contact angle and, for S_2, it even predicts a contact angle higher than the actual CB one. When the finite size of the droplet is taken into account, as done in Equation (2.5) and (2.4), the solution for the CB does not change but the W curve shifts to smaller values. This simple correction captures the overall trend with interpillar distance and improves the agreement with the global minima, although it is not quantitative. However, we remark that the finite size is not enough to account for the existence of multiple minima, which is due to pinning at individual pillars and is crucial to account for contact angle hysteresis.

In a nutshell, Monte Carlo, in combination with the string method, yields different

contact angles which could be measured in an actual experiment and provides a numerical evidence that Wenzel and similar models based on the homogenization of interfacial energies, overlook a crucial element to determine contact angle hysteresis, i.e., the distortions of the three-phase contact line.

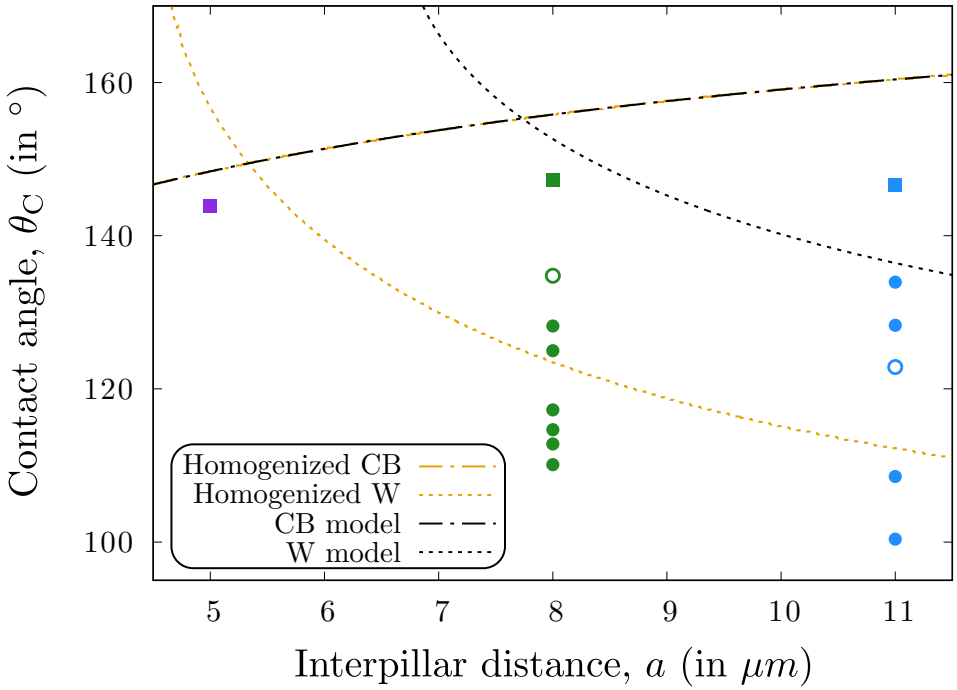

Figure 3.8: Apparent contact angle computed at physical minima in Figure 3.2 as a function of the distance between pillars. Squares are θ_C of the CB state, circles for the W minima; the open circles denote the global W minimum. Orange lines are the solution for the homogenized models: dot-dashed for CB, Equation (2.5), and dotted for W, Equation (2.4). Black lines are the predictions of the classical models: dot-dashed for CB, Equation (2.2), and dotted for W, Equation (2.1).

Figure 3.8 confirms that the extent of CAH has the following trend $S_1 < S_2 < S_3$, which suggests that the more favorable the W state, the higher θ_H. This trend is related to the number of local minima and to the facility of wetting the bottom of the surface for short pillars, but what limits the total number of minima still remains an open question. This is further discussed in the Perspectives section in Chapter 5.

Chapter 4

Results and Discussion: water/oil separation

In this Chapter we analyze the Monte Carlo simulation results for a mixed droplet on a pillared and porous surface. We compare these results with the theoretical predictions from the homogenized model and discuss the efficiency of these two types of surfaces in separating water from oil.

4.1 Pillared surface

The wetting diagram presented in Chapter 2, and repeated here in Figure 4.1, shows that a water droplet placed on a pillared surface can present a CB or a W state depending on the surface parameters. As previously explained, these wetting states are associated with a hydrophilic and hydrophobic behaviors respectively. On the other hand, for any geometric parameter, Figure 4.1-b shows that a droplet of pure oil will always present an oleophilic wetting state. Then, we expect that the pillared surfaces could work as an oil removing material in the region where a pure water droplet is in a CB state. If this is the case, these substrates would act as "sponges", absorbing oil and leaving water above the pillars.

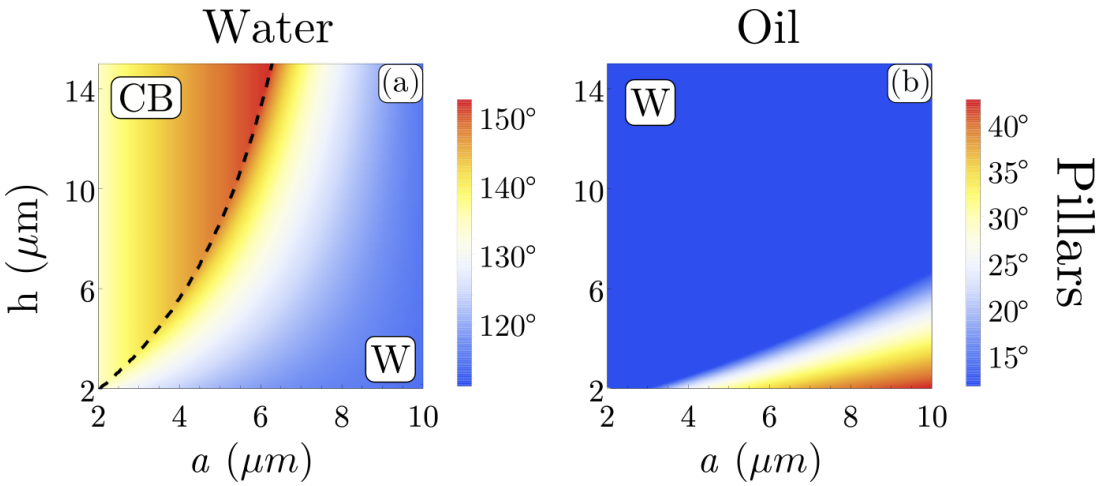

Figure 4.1: Theoretical wetting diagrams for **(a)** water droplet and **(b)** oil droplet placed on a pillared surface as a function of the pillar height h, and the interpillar distance a. Pillars width w $= 5\mu m$ and droplet radius $R = 50\,\mu$m are kept constant. The solid line in **(a)** represents the predicted thermodynamic transition between the Cassie-Baxter (CB) and Wenzel (W) states. Colors indicate the droplet contact angle, in degrees. Figure adapted from [22].

With that in mind, we performed several Monte Carlo simulation ranging over different values for the interpillar distance a while maintaining the width at a constant value w $= 5\,\mu$m and pillar height h $= 10\,\mu$m.

Figure 4.2-a shows the volume between the pillars v_p^{L} (L is the liquid type: w for water and o for oil) as a function of a for a drop composed mostly of water $f_o = 0.10$ and one composed mostly of oil $f_o = 0.90$, Figure 4.2-b. Panels **(c)**-**(f)** show the *lateral view* of the droplet configuration in the final wetting state correspondent to two different pillar distance, $a = 2\,\mu$m and $a = 14\,\mu$m, for each f_o. The vertical gray dotted lines shown in panels **(a)** and **(b)** indicate the water CB-W transition predicted by the theoretical homogenized model for the correspondent water volume. The value of interpillar distance a for which the CB-W transition occurs varies with the droplet initial volume (see Appendix B for more details).

The available volume to absorb oil is the maximum volume between pillars, given by $V_{\max} = \left(\frac{L_s}{\mathrm{d}}\right)^2 (\mathrm{d}^2 - \mathrm{w}^2)\mathrm{h}$, where L_s is the system size. The adimensional quantity $V_{\max}/V^o$, where V^o is the total oil volume present in the droplet, is shown in Figure 4.2-b by the gray dashed line. For the case of $f_o = 0.10$ the curve is not shown due to the fact that $V_{\max} \gg V^o$ for all values of a.

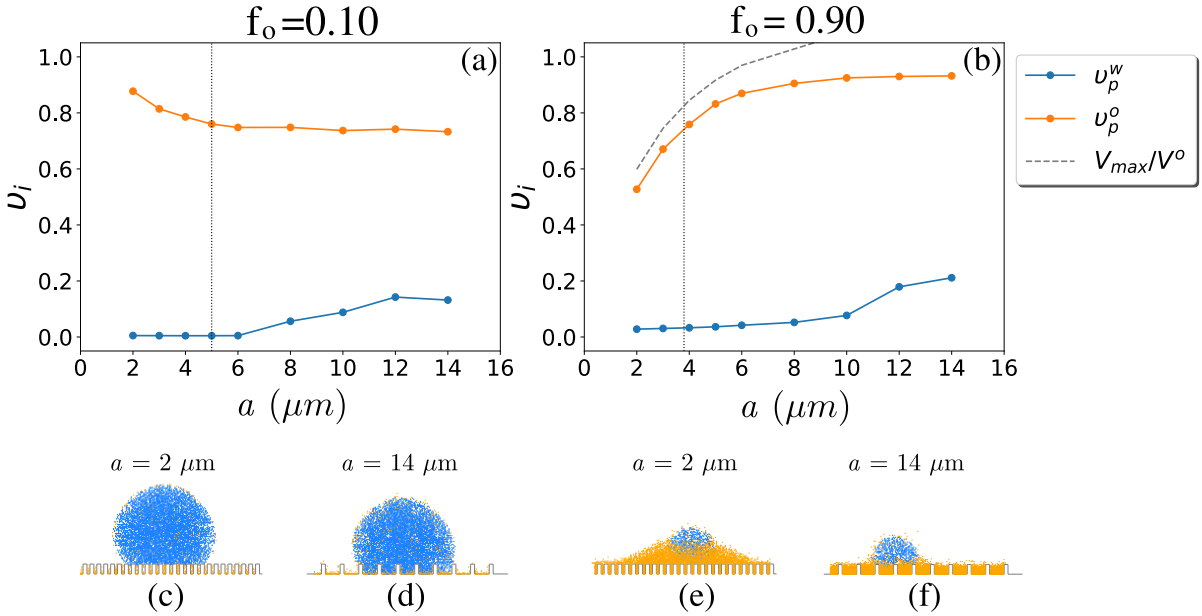

Figure 4.2: Results for pillared substrates. Above: Interpillar volume of water, υ_p^w, and oil, υ_p^o, as a function of the pillar distance a for **(a)** $f_o = 0.10$ and **(b)** $f_o = 0.90$. **(c)**-**(f)** Lateral view of the droplet configuration for $a = 2\mu$m and $a = 14\mu$m for each corresponding f_o. The mixed droplet was initialized with oil fraction given by f_o (value specified above the figures) and $R_0 = 50\mu$m. The pillared surface have fixed width w = 5μm and height h = 10μm. Blue color represents water and orange represents oil. Dotted lines represent the CB-W transition predicted by the theoretical model and the dashed line represents the maximum volume available between pillars $V_{\max}$ divided by the total oil volume, V^o.

For both cases we observe that the water does not penetrates the surface $\upsilon_p^w \approx 0$ (Figures 4.2-a,b) in the region of low interpillar distance. This result is consistent with the CB state predicted by the homogenized model. Then, as a increases, υ_p^w also increases, which roughly coincides with the theoretical prediction from CB to W states, indicated by the vertical dotted gray line. The visualization of the droplets confirms this behavior, where the water is in the CB state, panels **(c)** and **(e)**, for the case $a = 2\mu$m and in the W state for the case $a = 14\mu$m, panels **(d)** and **(f)**.

The particular case in which the droplet is composed mostly of water ($f_o = 0.10$) has a nice agreement between the predictions of the homogenized model and the MC simulation. For the case of $f_o = 0.90$ however, the transition from CB to W occurs for higher values of a, which does not agree with the predicted results. This difference is expected because the interaction between water and oil is not accounted for in the homogenized model.

For the case of oil, theoretical calculations show that a pure oil droplet does not

undergo any wetting state transition, remaining in the W state independently on the value of a. This is qualitatively confirmed by simulations, as shown by the oil penetration in Figures 4.2-a,b. For $f_o = 0.10$ and low values of a, υ_p^o indicates that 88% of the initial oil volume penetrates the substrate. As a increases, the percentage decreases and a plateau is observed at $\upsilon_p^o \approx 0.73$. For the case with $f_o = 0.9$ we observe an increase of υ_p^o with the increase of a and the plateau is reached at $\upsilon_p^o \approx 0.93$. This change in the oil absorption behavior is due to the increasing available volume between the pillars, $V_{\max}$. For lower values of interpillar distance, the pillared surface has space to accommodate roughly 60% of the initial oil volume, as indicated by the dashed gray line, resulting in a reduced oil absorption capacity and the saturation of the substrate. Increasing a also increases the available volume, $V_{\max}$, and a better oil absorption capacity is observed.

Despite the high percentage of the oil absorbed by the surface, we note that from 7% to 27% of the oil volume remains above the surface. This happens because the oil forms a film around the reminiscent water droplet, phenomena also observed experimentally [78, 79].

To understand this feature in our simulations, we have analyzed the terms of Equation (2.19) related to the energy for creating interfaces and evaluated the necessary conditions for the appearance of a site of type "oil" on the interface between the water and the gas. The calculations and more detailed arguments are discussed in Appendix B. This analysis led to two main conclusions: **(i)** the presence of an oil site on the interface of the droplet is favored when there are other oil sites surrounding it, suggesting that in the experiment, the oil could form a film on that interface and **(ii)** the formation of the oil film prevents a water-gas interface that is energetically unfavorable due to the relation between the surface tension values.

To end this section, we discuss the efficiency of this type of substrate using three different definitions introduced in Section 2.4.1. We compute $\xi^{\mathbf{a}}_{\mathbf{pil}}$, defined in Equation (2.25), which measures the amount of water that is not absorbed by the surface and $\xi^{\mathbf{r}}_{\mathbf{pil}}$, defined in Equation (2.27), that measures the capacity of the surface to exclude oil from the water remaining above the surface. We compare these quantities with the proposed separation efficiency given by the Equation (2.24), which takes into account both the capacity of maintaining water above the substrate and the capacity of absorbing oil.

Figure 4.3 summarizes our results of the surface efficiency in separate a droplet of water and oil. For both values of f_o, $\xi^{\mathbf{a}}_{\mathbf{pil}}$ follows the behavior of water: it shows a high efficiency when the water is in the CB state and decays when the transition to W occurs. On the other hand, $\xi^{\mathbf{r}}_{\mathbf{pil}}$ follows roughly the behavior of the oil where the efficiency is high

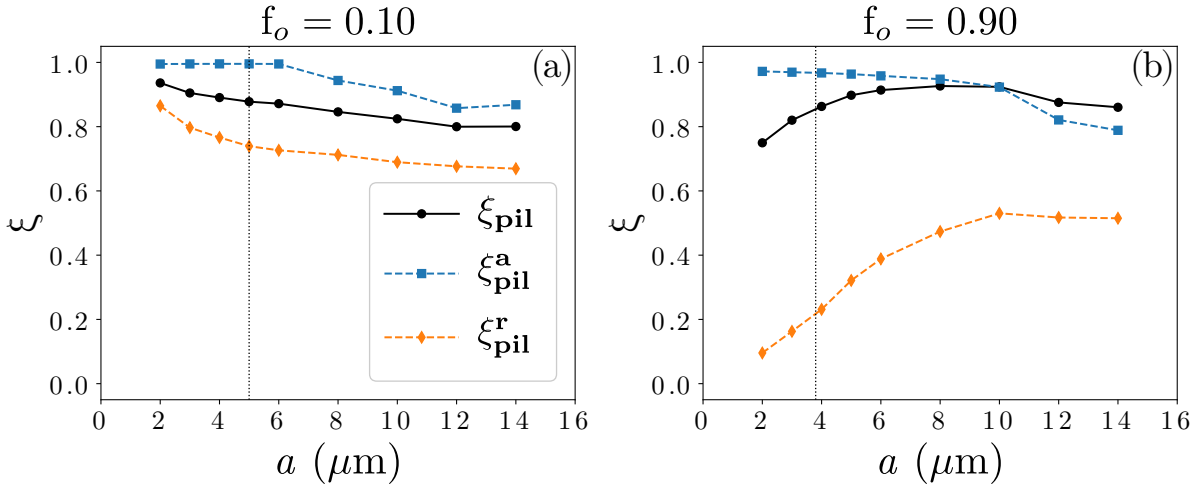

Figure 4.3: Efficiency for pillared substrates. $\xi^{\mathbf{a}}_{\mathbf{pil}}$, $\xi^{\mathbf{r}}_{\mathbf{pil}}$ and $\xi_{\mathbf{pil}}$ as a function of interpillar distance a for **(a)** $f_o = 0.10$ and **(b)** $f_o = 0.90$. Dotted lines represent the CB-W transition predicted by the homogenized model.

for surfaces where the percentage of oil that penetrates the surface (v_p^o) is also high.

The disadvantage of these definitions of efficiency is that it considers only one aspect of the separation process: the absorption of oil *or* the amount of water that remains in the surface. In the case of $f_o = 0.90$ and $a = 2\mu$m, $\xi^{\mathbf{a}}_{\mathbf{pil}}$ indicates an efficiency of this substrate of approximately 100% despite the fact that about 50% of the oil remains above the surface, as shown in Figure 4.2-e. In other words, $\xi^{\mathbf{a}}_{\mathbf{pil}}$ is high since there is no absorption of water by the substrate, but it is misleading because the oil remains above the surface too, which means that the separation of water and oil is not as good as its high value may suggest at first glance. On the other hand, $\xi^{\mathbf{r}}_{\mathbf{pil}}$ has a low value despite the fact that around 60% of the oil is wetting the surface and almost the whole amount of initial water remains above the substrate.

The definition of efficiency $\xi_{\mathbf{pil}}$ introduced in Section 2.4.1 takes into account both the water retention above the substrate *and* the oil absorption, which are the mechanisms that contributes to the water/oil separation. Thus, considering the same case of $f_o = 0.90$ and $a = 2\,\mu$m discussed above, $\xi_{\mathbf{pil}}$ is lower than $\xi^{\mathbf{a}}_{\mathbf{pil}}$ because it considers the reminiscent oil above the surface, while $\xi_{\mathbf{pil}}$ is greater than $\xi^{\mathbf{r}}_{\mathbf{pil}}$ because it considers the quantity and purity of the absorbed oil.

Despite the good efficiency observed, the pillared surface has the limitation of only been able to absorb a certain volume of oil, $V_{\mathbf{max}}$. In the next section we evaluate the performance of a surface which, in principle, do not have this problem.

4.2 Porous surface

In this section we consider a porous substrate where the oil can be drained into a reservoir. Here we explore this surface for the same oil fractions f_o considered for the pillar surface and surface parameters w = 5μm, h = 10μm and several values of porous distance a. According to the theoretical predictions from the homogenized model, repeated here in Figure 4.4, for pure water or pure oil, there is no wetting transition: the porous surface is hydrophobic and oleophilic for all considered values of geometric parameters.

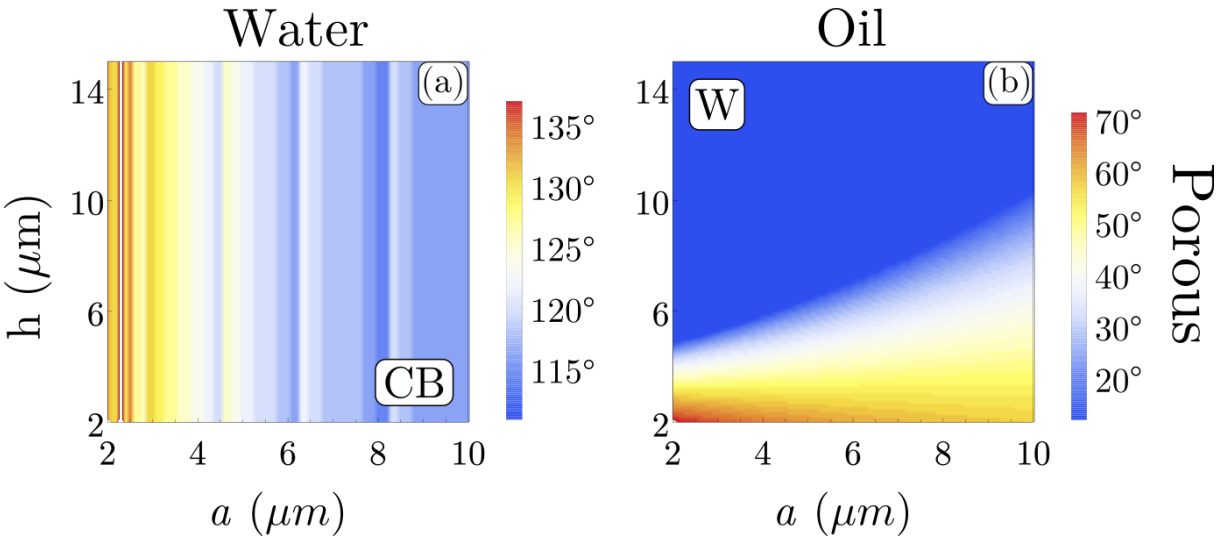

Figure 4.4: Theoretical wetting diagrams for **(a)** water droplet and **(b)** oil droplet placed on a porous surface as a function of the depth of the pore h, and the interporous distance a. The width w = 5 μm and droplet radius $R = 50\,\mu$m are kept constant. Colors indicate the droplet contact angle, in degrees. Figure adapted from [22].

Figure 4.5 shows the interporous percentage volume v_p^{L} and the reservoir percentage volume v_r^{L} as a function of porous distance a for two oil fractions, $f_o = 0.10$ and $f_o = 0.90$. For this type of surface, the volume normalization is such that $\mathrm{V}_p^{\mathrm{L}} + \mathrm{V}_r^{\mathrm{L}} + \mathrm{V}_a^{\mathrm{L}} = V^{\mathrm{L}}$ where $\mathrm{V}_a^{\mathrm{L}}$ is the remaining volume above the surface. For water, we observe that $v_p^w \approx 0$ and $v_r^w \approx 0$ for all geometric parameters and oil fractions considered, which means that water remains above the surface and do not penetrates the porous or the reservoir. This agrees with the results from the homogenized model for a droplet of pure water on porous substrates, shown in Figure 4.4-a, which predicts a hydrophobic wetting state for all geometric parameters.

Concerning the oil behavior, Figure 4.5 shows its presence in the pores v_p^o and in the reservoir v_r^o separately and also the sum of both contributions. The maximum available

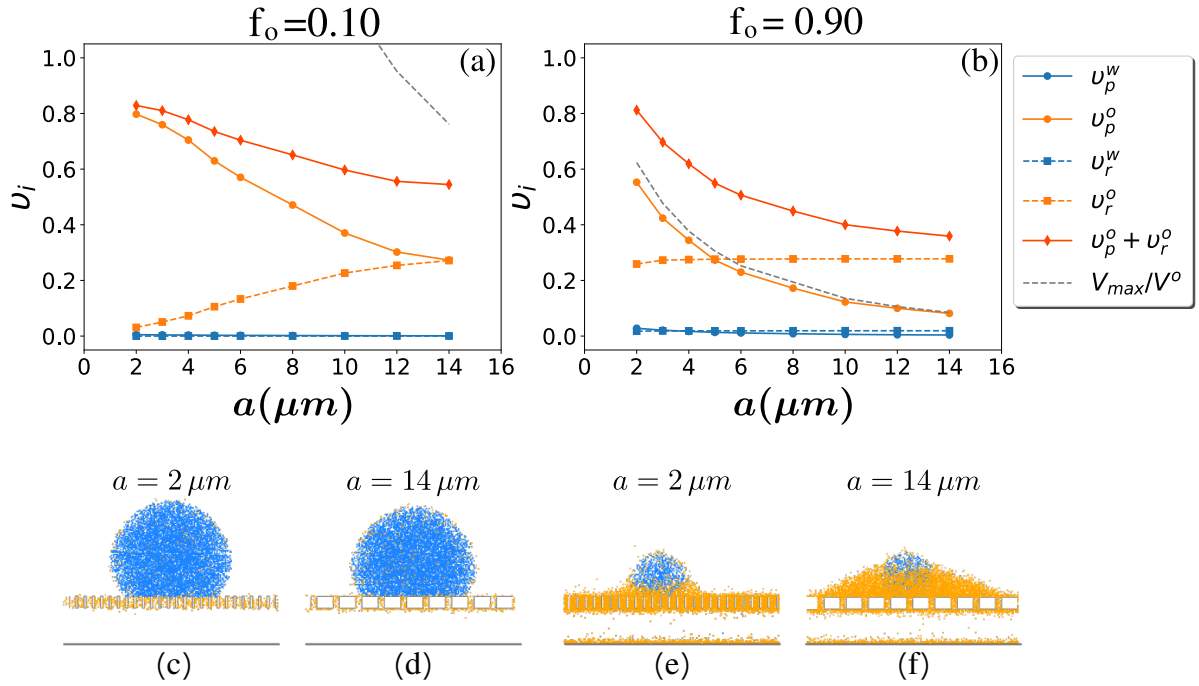

Figure 4.5: Results for porous substrates for several geometric parameters. Above: interporous volume of water υ_p^w and oil υ_p^o and reservoir volume of water υ_r^w and oil υ_r^o as a function of a for **(a)** $f_o = 0.10$ and **(b)** $f_o = 0.90$. Below: lateral view of the final droplet configuration for $a = 2\,\mu$m and $a = 14\,\mu$m for the corresponding f_o. The mixed droplet was initialized with oil fraction given by f_o (value specified above the figures) and $R_0 = 50\mu$m. The porous surface have fixed width w = 5μm and depth h = 10μm. Blue color represents water and orange represents oil. Dashed lines represent the maximum volume available between porous $V_{\max}$ divided by the total oil volume, V^o.

volume to absorb oil for the porous case is given by $V_{\max} = \left(\frac{L_s}{\mathrm{d}}\right)^2 \mathrm{hw}^2$. This quantity is divided by the initial oil volume in the droplet and is represented in Figure 4.5 by a dashed gray line.

Two aspects dictates the oil behavior for the porous surface: **(i)** the available volume inside the pores and **(ii)** the solid surface area above and below the substrate. For small values of a there is more interporous volume available for the oil and a smaller solid surface above and below the substrate, thus the oil remains inside the pores. As a increases, υ_p^o decreases due to the limited volume of the porous and υ_r^o increases due to the increase of the solid surface. However, the increase of the solid surface allows for a formation of an oil film on the surface as well, which jeopardize the entry of the oil in the reservoir. Since gravity does not play any role for this volume size, once the porous are filled with oil, it creates a layer that prevent the rest of oil to be absorbed and stored in the reservoir. The formation of a film in the interface between water and gas is also observed for the pillared surface.

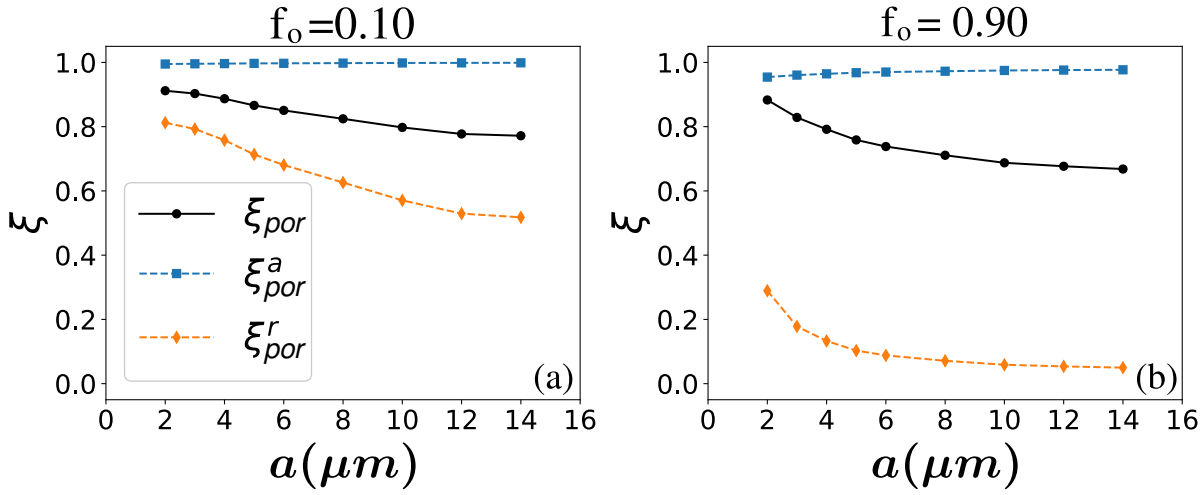

Figure 4.6: Efficiency for the porous surface. $\xi^{\mathbf{a}}_{\mathbf{por}}$, $\xi^{\mathbf{r}}_{\mathbf{por}}$ and $\xi_{\mathbf{por}}$ as a function of interpillar distance a for **(a)** $f_o = 0.10$ and **(b)** $f_o = 0.90$.

Figure 4.6 shows the efficiency of these surfaces in terms of the three measures defined in Equations (2.24), (2.26) and (2.28). Similarly to the discussion for the pillar substrates, $\xi^{\mathbf{a}}_{\mathbf{por}}$ and $\xi^{\mathbf{r}}_{\mathbf{por}}$ follow the behavior of the water and oil absorption respectively. In other words, these quantities only reflect the hydrophobicity *or* oleophilicity of the substrate and, therefore, they ignore part of the relevant mechanisms involved in water/oil separation. The alternative definition $\xi_{\mathbf{por}}$ takes into account both the hydrophobicity and oleophilicity by considering the total of oil present in the droplet to define an efficiency.

Chapter 5

Conclusion and Outlook

From self cleaning devices to the increase of energy efficiency of solar power cells, understanding the *wetting* properties of hydrophobic surfaces is crucial to the development of next-generation technologies. In this work, we proposed a study of two aspects of the wetting phenomenology: the fundamental characterization of the free energy landscape of a water droplet on a pillared surface, and the purification of a mixed droplet composed of water and oil.

To this end, we applied two methods: the first is an analytical approach of the global energy of the system, which we referred to as *homogenized approach*. It consists of calculating the energy cost of having a droplet in two wetting states, Cassie-Baxter (CB) and Wenzel (W) and, by comparing them, define the thermodynamic stable state. One of the drawbacks of this approach is that it cannot reproduce important features, such as the metastability of the CB state or the presence of many local minima related to the W state. The second method, which addresses this limitation, is a restrained Monte Carlo simulation of the cellular Potts model combined with the string method. The restrained MC allows to better explore the phase space, while the string method is an optimization tool that selects the best path for the exploration. We then use Thermodynamic Integration to calculate the free energy profile $\Delta\mathcal{F}$.

From previous numerical [45, 68] and experimental [5, 52, 54] works, metastability was known to be present in such systems. Using the numerical tools presented in Chapter 2, we found that the computed free energy landscape for wetting the surface has a complex behavior, with one minimum corresponding to the superhydrophobic Cassie-Baxter state; depending on the distance between the pillars, multiple local minima can exist, and are characterized by an increasing number of filled cavities, corresponding to different apparent contact angles. This scenario accounts for the strong contact angle hysteresis

found experimentally for the W state(s), in which the final wetting state depends on the initial condition, i.e., on fine details of the experimental procedure. Moreover, the free energy barriers between minima are typically much larger than thermal fluctuations, suggesting that mechanical vibrations of the substrate, for instance, are necessary to drive the droplet across different minima.

We have compared the apparent contact angles obtained in our *in silico* experiments with the predictions of simple models, including the classical Cassie-Baxter [43] and Wenzel [2] ones. Results showed that the Cassie-Baxter model has a good prediction capacity, which can be improved by considering the curvature of menisci overhanging on the surface. On the other hand, the prediction of the apparent contact angle cannot be made by simple models in the W state, which makes the deduction of surface features from θ_{C} more difficult. We focus, instead, on assessing the contact angle hysteresis, which can be achieved only by detailed models. In summary, we have found that by increasing the roughness of the surface, the CAH also increases, suggesting that the contact angle depends on the initial experimental setup, which is in agreement with previous studies [75, 76].

For the case of a mixed droplet, we use the homogenized approach to predict its behavior on top of a pillared and porous surface. Assuming that a appropriate material for separating oil from water would be simultaneously oleophilic and hydrophobic, the wetting diagram guides us in choosing the adequate type of substrate and its range of parameters. With this procedure we find that both pillared and porous surfaces are adequate for this purpose. Another drawback of this approach is that it cannot calculate the water-oil interaction. We then apply MC simulation of the four-state version of the CPM, which accounts for the interaction between the two liquids, to simulate surfaces with the selected parameters.

The behavior of the water contained in the droplet can be predicted by the wetting diagram, while the oil has a more complex behavior. Part of this complexity is due to the appearance of an oil film between the water and the gas. From these results, we calculate the efficiency of the surface in the separation of water and oil. Experimental works usually calculate the efficiency using one of the two following concepts: the first is based in the amount of water that remains above the surface [63, 64], while the second is based in the capacity of the surface to repel the oil [65, 66]. Our proposed method to calculate the efficiency takes into account both contributions simultaneously. We found that, a tightly packed pillared surface is more efficient in the separation of water and oil when the droplet is mostly composed by water. In contrast, when the droplet is mostly composed by oil, the separation efficiency increases when the pillars are sparsely distributed. In the case

of a porous surface, a small separation between the pores results in a higher capacity of separating water and oil, regardless of the composition of the droplet.

In summary, the combination of the two methods (i.e., homogenized approach and Monte Carlo simulations) presents a versatile and appropriate tool to understand open questions in the field of wetting. In the following we briefly elaborate possible future projects.

Perspectives

An interesting and long-standing question is the possibility of predicting CAH [80, 81, 82], which was possible for individual surfaces within our approach. Our analysis suggests that larger drops would have liquid enough to fill more cavities and thus the free energy profile would likely show even more local minima. What limits the total number of filled cavities and how these local minima connect to CAH could be investigating by applying the numerical methods for larger droplets.

Multiscale surfaces, such as fractals or simple and double reentrance, are known to present a more robust hydrophobic behavior [8, 70, 83]. Using the tools presented in this thesis we should be able to calculate the free energy of these surfaces and confirm that adding multiscale roughness to the surface increases the energy barrier.

Harvesting water from dried environment has been a fast growing research topic in the last years [84, 85, 86]. A beetle called *Stenocara gracilipes* is able to harvest water from such environment using its unique exoskeleton, which combines a hydrophobic and hydrophilic pattern. Based on this insect, we could employ the numerical tools to model a chemically heterogeneous surface and thus find the optimal relation between the two surface components (hydrophobic and hydrophilic) to maximize the water extraction.

Appendix A

Minimization process

In Chapter 2 we have introduced a model which takes into account the energy of creating interfaces of a 3D droplet with fixed volume $V_0 = 4/3\pi R_0^3$ when it is placed on a textured substrate. From the thermodynamic point of view, the stable wetting state is the one that has the smallest energy. In this appendix we detail the minimization process used to find the stable state for a droplet of water on a surface with a specific set of geometric parameter.

The droplet is allowed to display two wetting states, refereed as CB and W. For completeness, we repeat the expressions of the energy equation for both of this states for the case of a droplet on a pillared surface:

$$\Delta E_{\mathbf{pil}}^{\mathrm{CB}} = \mathrm{N}^{\mathrm{CB}} \left[(\sigma_{\mathrm{SL}} - \sigma_{\mathrm{SG}})\mathrm{w}^2 + (\mathrm{d}^2 - \mathrm{w}^2)\sigma_{\mathrm{GL}}\right] + \sigma_{\mathrm{GL}} S_{\mathrm{cap}}^{\mathrm{CB}}, \tag{A.1}$$

$$\Delta E_{\mathbf{pil}}^{\mathrm{W}} = \mathrm{N}^{\mathrm{W}} \left[(\mathrm{d}^2 + 4\mathrm{hw})\,(\sigma_{\mathrm{SL}} - \sigma_{\mathrm{SG}})\right] + \sigma_{\mathrm{GL}} S_{\mathrm{cap}}^{\mathrm{CB}}, \tag{A.2}$$

where $S_{\mathrm{s}} = 2\pi {R^{\mathrm{s}}}^2 \left[1 - \cos(\theta_{\mathrm{C}}^{\mathrm{s}})\right]$ is the surface of the spherical cap in contact with air, $B^{\mathrm{s}} = R^{\mathrm{s}} \sin(\theta_{\mathrm{C}}^{\mathrm{s}})$ is the base radius, R^{s} the radius of the droplet, and $\theta_{\mathrm{C}}^{\mathrm{s}}$ its contact angle in the state s (CB or W). The width of the pillar is given by w, pillar distance a, height h and $\mathrm{d} = \mathrm{w} + a$.

To identify the stable wetting state s between W and CB, we minimize Equations (A.1) and (A.2) using an algorithm proposed previously [45, 23, 22] and outlined in the following. First, we fix the parameters of the pillared surface (a, w, h) and the parameters of the droplet (radius R_0, type of liquid θ_{Y} and σ_{GL}). Then, we vary θ_c^s to calculate the energies of the CB state, ΔE^{CB}, and W state, ΔE^{W} and find the minimum value of each one, $\Delta E_{\mathrm{min}}^{\mathrm{CB}}$ and $\Delta E_{\mathrm{min}}^{\mathrm{W}}$. Finally, we compare both minimum energy and find the lowest value to define the thermodynamic stable wetting state.

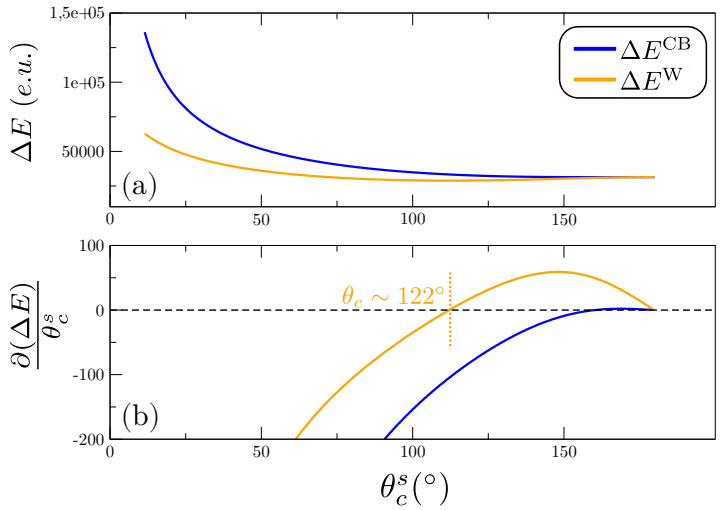

Figure A.1: **(a)** ΔE^{CB} in blue and ΔE^{W} in orange, as a function of contact angle θ_c^s. **(b)** Derivative of the energies as a function of θ_c^s. $\theta_{\mathrm{C}} = 122°$ corresponds to the contact angle of the W state, which is the wetting state that minimizes the energy of the droplet in this example.

Figure A.1-a shows an example for a pillared surface with parameters ($a = 11\,\mu$m, h $= 10\,\mu$m, $\theta_{\mathrm{Y}} = 114°$) on which a droplet of radius $R_0 = 50\,\mu$m is deposited. The numerical solution of ΔE^{CB} is shown in blue and ΔE^{W} in orange, as a function of θ_c^s. For this set of surface parameters, $\Delta E^{\mathrm{W}}_{\mathrm{min}} < \Delta E^{\mathrm{CB}}_{\mathrm{min}}$, which indicates that W is the stable state. Then, by deriving the energy in relation to θ_c^s, Figure A.1-b, we find the contact angle that minimizes that wetting state. For this surface, the droplet is in the W state with a contact angle given by $\theta_{\mathrm{C}} = 122°$.

Appendix B

Supplementary information for water/oil results

The choice of the parameter T is an important step in the simulation. We look for a values of T that fulfill two conditions: a) T cannot be large enough to evaporate the liquid (in this case the volume would not stay constant) and b) it cannot be too small, because it would in practice freeze the dynamics. In other words, the acceptance rate would become so small that it would be necessary a long-time simulations in order to observe any significant change.

Figure B.1-a shows the average acceptance ratio for a droplet with pure water ($f_o = 0$) and a droplet with pure oil ($f_o = 1$) as a function of T. In Figure B.1-b we show the average number of gas neighbors of the liquid site (water or oil). With these figures we reach the following conclusion: i) for $T > 10$ the acceptance rate reaches a plateau of $\sim 30\%$ for a droplet of oil. ii) in this same range the number of gas sites neighbors of a liquid site increases rapidly, meaning that each liquid site has only gas neighbors and indicating that the droplet had evaporated. iii) for $T < 7$ the acceptance ratio of a droplet of water is less than 10%. An acceptance ratio this low indicates that a long-time simulation is necessary to observe change in the droplet. Therefore, we select$T = 9$ as the parameter that fulfill both conditions.

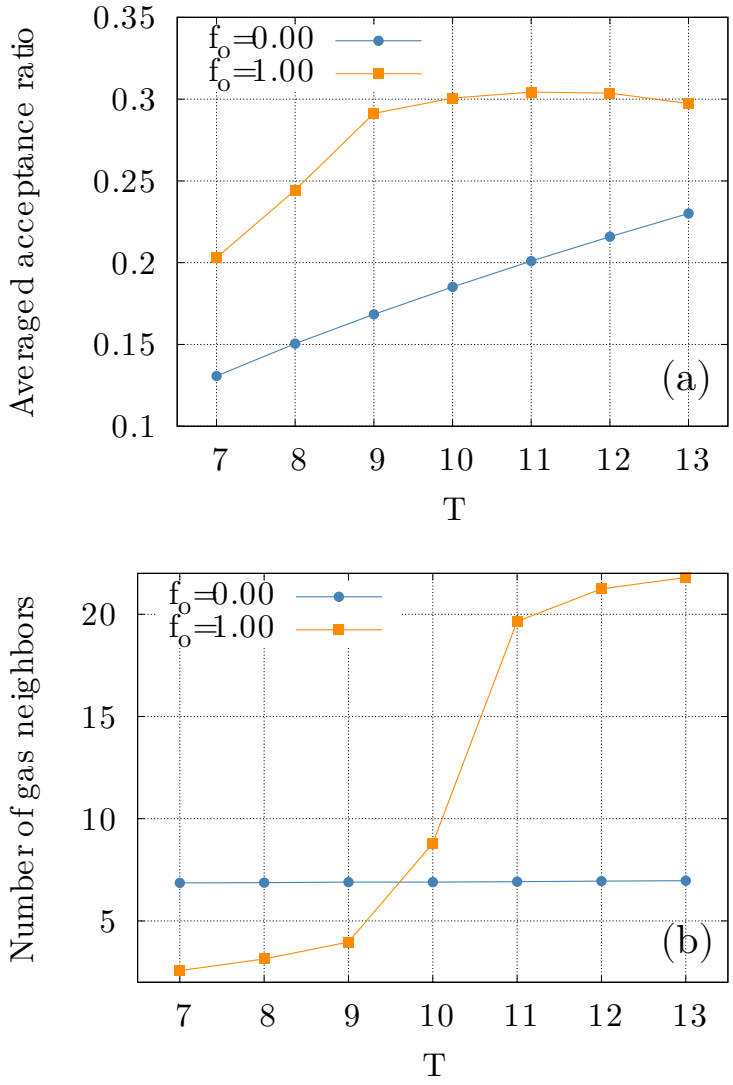

Figure B.1: **(a)** average acceptance ratio as a function of parameter T for a droplet of water ($f_o = 0$) and a droplet of oil ($f_o = 1$). **(b)** average number of neighbors of a liquid spin that have a gas neighbour.

B.1 Theoretical wetting diagram for different values of R_o.

The vertical dotted lines in Figure 4.2-a,b of Chapter 4 marks the point where a CB-W transition happens for a pillared surface in the theoretical homogenized model. This transition occurs for different values of interpillar distance a depending on the droplet size [45]. In order to obtain the point of transition we performed calculation using the homogenized model considering the volume of water present in a mixture droplet with $R = 50\mu$m and compositions given by $f_o = 0.10$ and $f_o = 0.90$. In other words we obtain

the wetting diagram for a pure water droplet with radius $R \approx 48.3\mu$m (same water volume as in the mixture oil/water droplet with $f_o = 0.10$) and $R \approx 23.2\mu$m (same water volume as in the mixture oil/water droplet with $f_o = 0.90$).

For a pillared substrate with h $= 10\mu$m and w $= 5\mu$m (horizontal gray line in Figure B.2) the transition from CB to W happens at $a \approx 3.9\mu$m for $f_o = 0.90$ and $a \approx 5\mu$m for $f_o = 0.10$. These the values are indicated by the vertical line in Figure 4.2-a,b in Chapter 4.

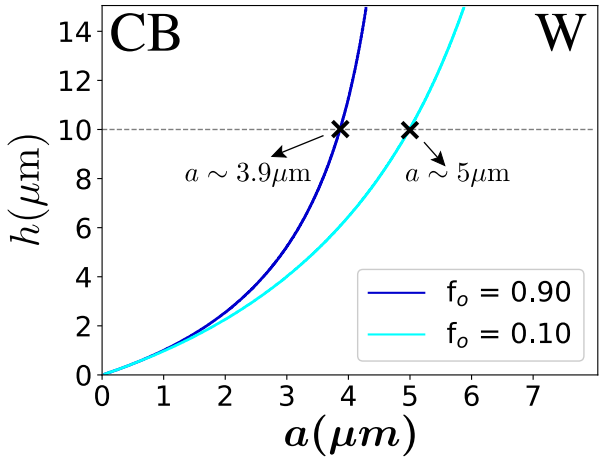

Figure B.2: Wetting diagram for a pure water droplet with $R_o \approx 48.3\mu$ (same water volume as the mixture oil/water droplet with $R_o = 50\mu$m and oil fraction $f_o = 0.10$) and $R_o \approx 23.2\mu$ (same water volume as the mixture oil/water droplet with $R_o = 50\mu$m and oil fraction $f_o = 0.90$).

B.2 Calculation and discussion about the oil film formation

We first consider a spin i with state gas G that is on the interface of the droplet and has n_O^i neighbors of type "oil", n_G^i neighbors of type "gas" and n_W^i neighbors of type "water". The flip of this spin i from a gas to oil state is energetically favored when:

$$n_O^i > n_G^i - n_W^i \frac{(\sigma_{GW} - \sigma_{WO})}{\sigma_{GO}}. \tag{B.1}$$

This lead to two conclusions: (i) The presence of oil is favorable when the site i is surrounded by other sites of type oil. It shows that for the oil on the interface is favorable to form a cluster or a film. (ii) Even if the site i has no oil neighbor, $n_O^i = 0$, the presence of the oil is energetically favorable when $n_G^i < n_W^i((\sigma_{GW} - \sigma_{WO})/\sigma_{GO})$. This last condition is

satisfied when $\sigma_{\mathrm{GW}} > \sigma_{\mathrm{WO}}$, which is always the case in our calculations (see Section 2.2 for the numerical values). Physically, it tells us that the appearance of a oil on the interface can happen because σ_{GW} is high compared to σ_{WO}. This suggests that changing the gas in such way to increase σ_{WO} and/or decrease σ_{GW} could improve the capacity of separating oil and water.

A similar calculation can be done for the case where the site i is in the water state. The condition in which the change to a oil state is energetically favorable is $\mathrm{n_O^i} > \mathrm{n_W^i} - \mathrm{n_G^i}((\sigma_{\mathrm{GW}} - \sigma_{\mathrm{GO}})/\sigma_{\mathrm{WO}})$. The analysis of this equation leads to the same conclusions described above.

B.3 Results for the surfaces with $\mathbf{h = 5\mu m}$

In this section we show the simulations results for the pillared surface and porous surface with $\mathrm{h} = 5\mu\mathrm{m}$. Figures B.3-a,b show the percentage of volume between the pillars for the water component υ_p^w and for the oil component υ_p^o as a function of the interpillar distance a. On the left are the results for a droplet composed mostly of water ($\mathrm{f}_o = 0.10$) and on the right for a droplet composed mostly of oil ($\mathrm{f}_o = 0.90$).

Similar to the results for $\mathrm{h} = 10\mu m$, we observe that the water does not penetrate the surface, $\upsilon_p^w \approx 0$, when the interpillar distance is low. As a increases, there is a slight increase in the water that wets the surface and, for this case, it does not coincide with the theoretical prediction for the transition between CB and W states. Again, we note that although the MC simulation does take into account the interaction between water and oil, the homogenized model does not, so differences between the two approaches are expected.

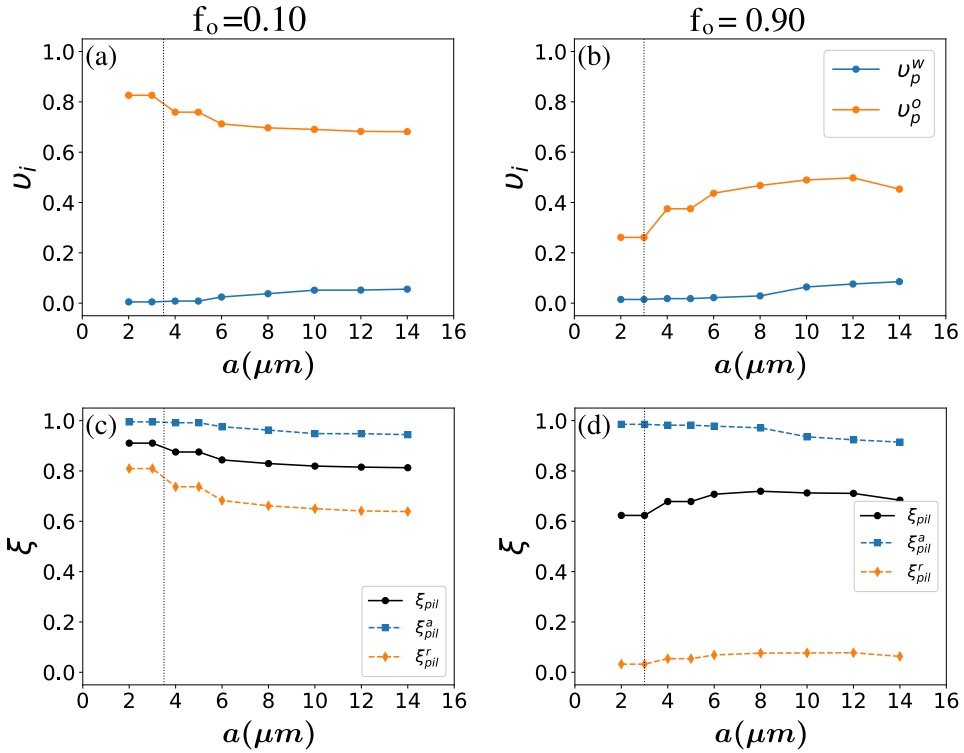

Figure B.3: **Results for pillared substrates.** Interpillar volume of water, υ_p^w, and oil, υ_p^o, as a function of the pillar distance a for **(a)** $f_o = 0.10$ and **(b)** $f_o = 0.90$. Blue color represents water and orange represents oil. $\xi_{\mathbf{pil}}^{\mathbf{a}}$, $\xi_{\mathbf{pil}}^{\mathbf{r}}$ and $\xi_{\mathbf{pil}}$ as a function of a for **(c)** $f_o = 0.10$ and **(d)** $f_o = 0.90$. Dotted lines represent the CB-W transition predicted by the theoretical model.

Figures B.3-c,d compares the three efficiencies defined previously: $\xi_{\mathbf{pil}}^{\mathbf{a}}$, which measures the amount of water that is not absorbed by the surface, $\xi_{\mathbf{pil}}^{\mathbf{r}}$, which measures the capacity of the surface to exclude oil from the water remaining above the surface and $\xi_{\mathbf{pil}}$, a new proposed formula that takes into account both the capacity of maintaining water above the substrate and the capacity of absorbing oil. For the case f$_o$ = 0.90 and $a = 10\mu$m, $\xi_{\mathbf{pil}}^{\mathbf{a}}$ shows a high efficiency despite the fact that only around 50% of the oil is wetting the cavities. $\xi_{\mathbf{pil}}^{\mathbf{r}}$, on the other hand, shows a low efficiency even when almost all the water volume is above the surface. These measures can be misleading due to the fact that they take into account only aspect, the absorption of oil *or* the exclusion of water from the cavities. The proposed efficiency $\xi_{\mathbf{pil}}$ includes both of these aspects in the calculations.

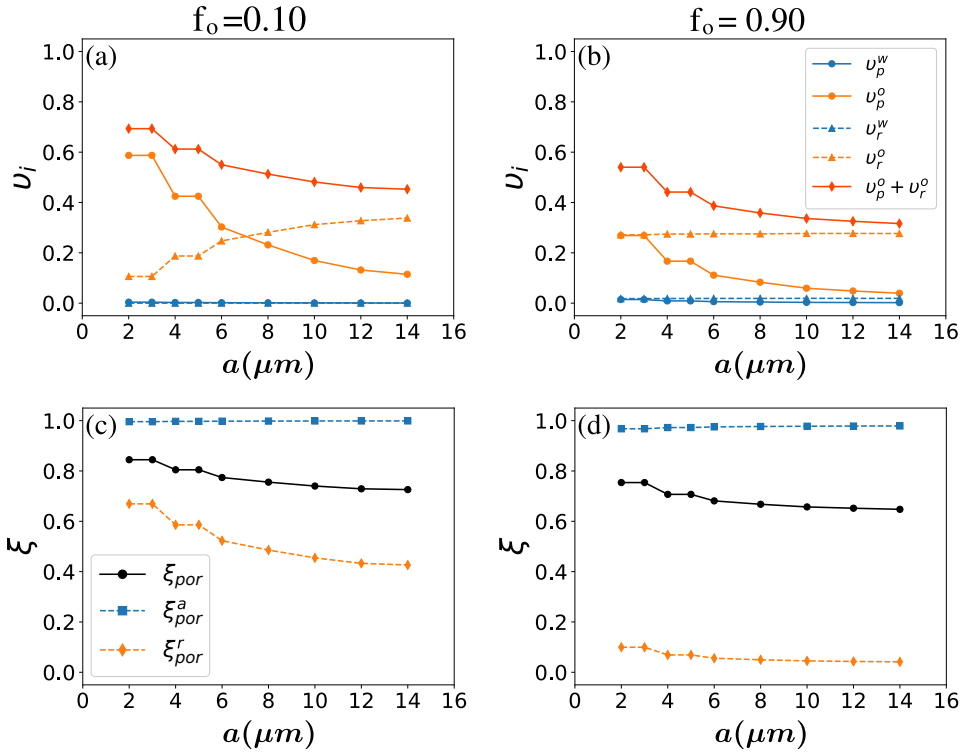

Figure B.4: **Results for porous substrates.** Interporous volume and reservoir volume of water, υ_p^w and υ_r^w, and oil, υ_p^o and υ_r^o, as a function of the porous distance a for **(a)** $f_o = 0.10$ and **(b)** $f_o = 0.90$. Blue color represents water and orange represents oil. $\xi^{\mathbf{a}}_{\mathbf{por}}$, $\xi^{\mathbf{r}}_{\mathbf{por}}$ and $\xi_{\mathbf{por}}$ as a function of a for **(c)** $f_o = 0.10$ and **(d)** $f_o = 0.90$.

In Figure B.4-a,b we observe that, for the porous surface, as a increases, the percentage of oil volume wetting the porous and the reservoir $\upsilon_p^o + \upsilon_r^o$ decreases. Then, since the efficiency $\xi^{\mathbf{r}}_{\mathbf{por}}$ follows the oil behavior, this value also decreases. For the water component, the homogenized approach predicted a CB (hydrophobic) wetting state for all values of a. This is confirmed by the simulation because $\upsilon_p^w + \upsilon_r^w \approx 0$ independently on the value of interpillar distance. Looking at $\xi^{\mathbf{a}}_{\mathbf{por}}$ in Figures B.4-c,d can lead to misleading conclusions, since the calculation of this efficiency does not include the oil that remains above the surface with the water.

Bibliography

[1] T. Young, "An essay on the cohesion of fluids," *Philosophical Transactions of the Royal Society of London*, vol. 95, pp. 65–87, 1805.

[2] R. N. Wenzel, "Resistance of solid surfaces to wetting by water," *Ind. Eng. Chem.*, vol. 28, no. 8, pp. 988–994, 1936.

[3] F. Bottiglione and G. Carbone, "An effective medium approach to predict the apparent contact angle of drops on super-hydrophobic randomly rough surfaces," *Journal of Physics: Condensed Matter*, vol. 27, no. 1, p. 015009, 2014.

[4] A. Bussonniere, M. B. Bigdeli, D.-Y. Chueh, Q. Liu, P. Chen, and P. A. Tsai, "Universal wetting transition of an evaporating water droplet on hydrophobic micro- and nano-structures," *Soft Matter*, vol. 13, pp. 978–984, 2017.

[5] M. Callies and D. Quéré, "On water repellency," *Soft matter*, vol. 1, no. 1, pp. 55–61, 2005.

[6] X. Chen, R. Ma, J. Li, C. Hao, W. F, B. L. Luk, S. C. Li, S. Yao, and Z. Wang, "Evaporation of droplets on superhydrophobic surfaces: surface roughness and small droplet size effects," *Phys. Rev. Lett.*, vol. 109, no. September, p. 116101, 2012.

[7] X. Chen, J. A. Weibel, and S. V. Garimella, "Water and ethanol droplet wetting transition during evaporation on omniphobic surfaces," *Scientific reports*, vol. 5, 2015.

[8] T. L. Liu and C. J. Kim, "Turning a surface superrepellent even to completely wetting liquids," *Science*, vol. 346, pp. 1096–1100, 2014.

[9] M. Costa, B. Veigas, J. Jacob, D. Santos, J. Gomes, P. Baptista, R. Martins, J. Inácio, and E. Fortunato, "A low cost, safe, disposable, rapid and self-sustainable paper-based platform for diagnostic testing: lab-on-paper," *Nanotechnology*, vol. 25, no. 9, p. 094006, 2014.

[10] "Nasa uses lotus leaf as inspiration for space gear dust-repellent." `https://www.treehugger.com/clean-technology/nasa-uses-lotus-leaf-as-inspiration-for-space-gear-dust-repellent.html`. Accessed: 31-07-2019.

[11] "Water spider (raft spider) by thomsonalasdair." `https://bighugelabs.com/onblack.php?id=237875014&bg=white&size=large`. Accessed: 23-08-2021.

[12] Y. Liu, S. Akin, L. Pan, R. Uchida, N. Arora, J. V. Milić, A. Hinderhofer, F. Schreiber, A. R. Uhl, S. M. Zakeeruddin, *et al.*, "Ultrahydrophobic 3d/2d fluoroarene bilayer-based water-resistant perovskite solar cells with efficiencies exceeding 22%," *Science advances*, vol. 5, no. 6, p. eaaw2543, 2019.

[13] H. Zhao and K. Y. Law, "Super toner and ink repellent superoleophobic surface," *ACS applied materials & interfaces*, vol. 4, no. 8, pp. 4288–4295, 2012.

[14] J. Drelich, E. Chibowski, D. D. Meng, and K. Terpilowski, "Hydrophilic and superhydrophilic surfaces and materials," *Soft Matter*, vol. 7, no. 21, pp. 9804–9828, 2011.

[15] M. Kawamura, "Filtration membrane for oleophilic organic liquids, method for producing it, and method for filtering oleophilic organic liquids," Aug. 3 1999. US Patent 5,932,104.

[16] Y. Cai, L. Lin, Z. Xue, M. Liu, S. Wang, and L. Jiang, "Filefish-inspired surface design for anisotropic underwater oleophobicity," *Advanced Functional Materials*, vol. 24, no. 6, pp. 809–816, 2014.

[17] T.-i. Kim, D. Tahk, and H. H. Lee, "Wettability-controllable super water-and moderately oil-repellent surface fabricated by wet chemical etching," *Langmuir*, vol. 25, no. 11, pp. 6576–6579, 2009.

[18] S. Nishimoto and B. Bhushan, "Bioinspired self-cleaning surfaces with superhydrophobicity, superoleophobicity, and superhydrophilicity," *Rsc Advances*, vol. 3, no. 3, pp. 671–690, 2013.

[19] J. Zhang and S. Seeger, "Superoleophobic coatings with ultralow sliding angles based on silicone nanofilaments," *Angewandte Chemie International Edition*, vol. 50, no. 29, pp. 6652–6656, 2011.

[20] A. Vilcnik, I. Jerman, A. Surca Vuk, M. Kozelj, B. Orel, B. Tomsic, B. Simoncic, and J. Kovac, "Structural properties and antibacterial effects of hydrophobic

and oleophobic sol- gel coatings for cotton fabrics," *Langmuir*, vol. 25, no. 10, pp. 5869–5880, 2009.

[21] M. Silvestrini, A. Tinti, A. Giacomello, and C. Brito, "Can one predict a drop contact angle?," *Advanced Materials Interfaces*, p. 2101005, 2021.

[22] C. Gavazzoni, M. Silvestrini, and C. Brito, "Modeling oil–water separation with controlled wetting properties," *The Journal of Chemical Physics*, vol. 154, no. 10, p. 104704, 2021.

[23] M. Silvestrini and C. Brito, "Wettability of reentrant surfaces: a global energy approach," *Langmuir*, vol. 33, no. 43, pp. 12535–12545, 2017.

[24] M. Xu, G. Sun, and C.-J. Kim, "Infinite lifetime of underwater superhydrophobic states," *Physical review letters*, vol. 113, no. 13, p. 136103, 2014.

[25] S. Bonella, S. Meloni, and G. Ciccotti, "Theory and methods for rare events," *The European Physical Journal B*, vol. 85, no. 3, pp. 1–19, 2012.

[26] M. Amabili, E. Lisi, A. Giacomello, and C. M. Casciola, "Wetting and cavitation pathways on nanodecorated surfaces," *Soft matter*, vol. 12, no. 12, pp. 3046–3055, 2016.

[27] M. Amabili, S. Meloni, A. Giacomello, and C. M. Casciola, "Activated wetting of nanostructured surfaces: reaction coordinates, finite size effects, and simulation pitfalls," *The Journal of Physical Chemistry B*, vol. 122, no. 1, pp. 200–212, 2017.

[28] A. Giacomello, S. Meloni, M. Müller, and C. M. Casciola, "Mechanism of the cassie-wenzel transition via the atomistic and continuum string methods," *The Journal of chemical physics*, vol. 142, no. 10, p. 104701, 2015.

[29] S. Schnabel and W. Janke, "Distribution of metastable states of ising spin glasses," *Physical Review B*, vol. 97, no. 17, p. 174204, 2018.

[30] T. Koishi, K. Yasuoka, and S. Fujikawa, "Coexistence and transition between Cassie and Wenzel state on pillared hydrophobic surface.," *Proc. Natl. Acad. Sci. U. S. A.*, vol. 106, no. 21, pp. 8435–8440, 2009.

[31] A. Giacomello, S. Meloni, M. Chinappi, and C. M. Casciola, "Cassie-baxter and wenzel states on a nanostructured surface: phase diagram, metastabilities, and transition mechanism by atomistic free energy calculations," *Langmuir*, vol. 28, no. 29, pp. 10764–10772, 2012.

[32] P. Tsai, R. G. H. Lammertink, M. Wessling, and D. Lohse, "Evaporation-triggered wetting transition for water droplets upon hydrophobic microstructures," *Phys. Rev. Lett.*, vol. 104, no. March, p. 116102, 2010.

[33] H. Huang, R. Joshi, K. D. Silva, R. Badam, and M. Yoshimura, "Fabrication of reduced graphene oxide membranes for water desalination," *Journal of membrane science*, vol. 572, pp. 12–19, 2019.

[34] Y. Yang, X. Yang, L. Liang, Y. Gao, H. Cheng, X. Li, M. Zou, R. Ma, Q. Yuan, and X. Duan, "Large-area graphene-nanomesh/carbon-nanotube hybrid membranes for ionic and molecular nanofiltration," *Science*, vol. 364, no. 6445, pp. 1057–1062, 2019.

[35] Y. Qian, X. Zhang, C. Liu, C. Zhou, and A. Huang, "Tuning interlayer spacing of graphene oxide membranes with enhanced desalination performance," *Desalination*, vol. 460, pp. 56–63, 2019.

[36] Z. Xue, Y. Cao, N. Liu, L. Feng, and L. Jiang, "Special wettable materials for oil/water separation," *Journal of Materials Chemistry A*, vol. 2, no. 8, pp. 2445–2460, 2014.

[37] Y. J. Chan, M. F. Chong, C. L. Law, and D. G. Hassell, "A review on anaerobic–aerobic treatment of industrial and municipal wastewater," *Chemical Engineering Journal*, vol. 155, no. 1-2, pp. 1–18, 2009.

[38] M. Padaki, R. S. Murali, M. S. Abdullah, N. Misdan, A. Moslehyani, M. Kassim, N. Hilal, and A. Ismail, "Membrane technology enhancement in oil–water separation. a review," *Desalination*, vol. 357, pp. 197–207, 2015.

[39] D. Sun, X. Duan, W. Li, and D. Zhou, "Demulsification of water-in-oil emulsion by using porous glass membrane," *Journal of membrane science*, vol. 146, no. 1, pp. 65–72, 1998.

[40] A. Cambiella, J. Benito, C. Pazos, and J. Coca, "Centrifugal separation efficiency in the treatment of waste emulsified oils," *Chemical Engineering Research and Design*, vol. 84, no. 1, pp. 69–76, 2006.

[41] T. Strøm-Kristiansen, A. Lewis, P. S. Daling, and A. B. Nordvik, "Heat and chemical treatment of mechanically recovered w/o emulsions," *Spill Science & Technology Bulletin*, vol. 2, no. 2-3, pp. 133–141, 1995.

[42] C. Chen, D. Weng, A. Mahmood, S. Chen, and J. Wang, "Separation mechanism and construction of surfaces with special wettability for oil/water separation," *ACS applied materials & interfaces*, vol. 11, no. 11, pp. 11006–11027, 2019.

[43] A. Cassie and S. Baxter, "Wettability of porous surfaces," *Trans. Faraday Soc.*, vol. 40, pp. 546–551, 1944.

[44] A. Shahraz, A. Borhan, and K. A. Fichthorn, "A theory for the morphological dependence of wetting on a physically patterned solid surface," *Langmuir*, vol. 28, no. 40, pp. 14227–14237, 2012.

[45] H. C. M. Fernandes, M. H. Vainstein, and C. Brito, "Modeling of droplet evaporation on superhydrophobic surfaces," *Langmuir*, vol. 31, no. 27, pp. 7652–7659, 2015.

[46] J. Yong, F. Chen, Q. Yang, J. Huo, and X. Hou, "Superoleophobic surfaces," *Chemical Society Reviews*, vol. 46, no. 14, pp. 4168–4217, 2017.

[47] F. Graner and J. A. Glazier, "Simulation of biological cell sorting using a two-dimensional extended potts model," *Phys. Rev. Lett.*, vol. 69, no. 13, pp. 2013–2017, 1992.

[48] L. R. de Oliveira, D. M. Lopes, S. M. M. Ramos, and J. C. M. Mombach, "Two-dimensional modeling of the superhydrophobic behavior of a liquid droplet sliding down a ramp of pillars," *Soft Matter*, vol. 7, pp. 3763–3765, 2011.

[49] D. M. Lopes, L. R. de Oliveira, S. M. M. Ramos, and J. C. M. Mombach, "Cassie-Baxter to Wenzel state wetting transition: a 2D numerical simulation," *Royal Society of Chemistry Advances*, vol. 3, pp. 24530–24534, 2013.

[50] R. Xu, X. Zhao, L. Wang, C. Zhang, Y. Mao, L. Shi, and D. Zheng, "A minimum energy optimization approach for simulations of the droplet wetting modes using the cellular potts model," *RSC Advances*, vol. 11, no. 3, pp. 1875–1882, 2021.

[51] S. Wang, H. Liu, D. Liu, X. Ma, X. Fang, and L. Jiang, "Enthalpy-driven three-state switching of a superhydrophilic/superhydrophobic surface," *Angewandte Chemie International Edition*, vol. 46, no. 21, pp. 3915–3917, 2007.

[52] M. Nosonovsky and B. Bhushan, "Biomimetic superhydrophobic surfaces: multiscale approach," *Nano Lett.*, vol. 7, pp. 2633–2637, 2007.

[53] M. Nosonovsky and B. Bhushan, "Patterned nonadhesive surfaces: superhydrophobicity and wetting regime transitions," *Langmuir*, vol. 24, no. 4, pp. 1525–1533, 2008.

[54] M. Sbragaglia, A. M. Peters, C. Pirat, B. M. Borkent, R. G. H. Lammertink, M. Wessling, and D. Lohse, "Spontaneous breakdown of superhydrophobicity," *Phys. Rev. Lett.*, vol. 99, no. October, p. 156001, 2007.

[55] J. Kästner, "Umbrella sampling," *Wiley Interdisciplinary Reviews: Computational Molecular Science*, vol. 1, no. 6, pp. 932–942, 2011.

[56] L. Maragliano, A. Fischer, E. Vanden-Eijnden, and G. Ciccotti, "String method in collective variables: Minimum free energy paths and isocommittor surfaces," *The Journal of chemical physics*, vol. 125, no. 2, p. 024106, 2006.

[57] M. Amabili, S. Meloni, A. Giacomello, and C. M. Casciola, "Activated wetting of nanostructured surfaces: reaction coordinates, finite size effects, and simulation pitfalls," *The Journal of Physical Chemistry B*, vol. 122, no. 1, pp. 200–212, 2018.

[58] A. Tinti, A. Giacomello, Y. Grosu, and C. M. Casciola, "Intrusion and extrusion of water in hydrophobic nanopores," *PNAS*, vol. 114, no. 48, pp. E10266–E10273, 2017.

[59] E. Darve and A. Pohorille, "Calculating free energies using average force," *The Journal of chemical physics*, vol. 115, no. 20, pp. 9169–9183, 2001.

[60] A. Laio and M. Parrinello, "Escaping free-energy minima," *Proceedings of the National Academy of Sciences*, vol. 99, no. 20, pp. 12562–12566, 2002.

[61] E. Weinan, W. Ren, and E. Vanden-Eijnden, "Simplified and improved string method for computing the minimum energy paths in barrier-crossing events," *J. Chem. Phys.*, vol. 126, no. 16, p. 164103, 2007.

[62] D. Frenkel and B. Smit, *Understanding molecular simulation: from algorithms to applications*, vol. 1. Elsevier, 2001.

[63] J. Gu, P. Xiao, J. Chen, F. Liu, Y. Huang, G. Li, J. Zhang, and T. Chen, "Robust preparation of superhydrophobic polymer/carbon nanotube hybrid membranes for highly effective removal of oils and separation of water-in-oil emulsions," *Journal of Materials Chemistry A*, vol. 2, no. 37, pp. 15268–15272, 2014.

[64] A. Singh and J. Singh, "Fabrication of zirconia based durable superhydrophobic–superoleophilic fabrics using non fluorinated materials for oil–water separation and water purification," *RSC advances*, vol. 6, no. 105, pp. 103632–103640, 2016.

[65] Z. Wang, C. Xiao, Z. Wu, Y. Wang, X. Du, W. Kong, D. Pan, G. Guan, and X. Hao, "A novel 3d porous modified material with cage-like structure: fabrication and its demulsification effect for efficient oil/water separation," *Journal of Materials Chemistry A*, vol. 5, no. 12, pp. 5895–5904, 2017.

[66] M. Su, Y. Liu, S. Li, Z. Fang, B. He, Y. Zhang, Y. Li, and P. He, "A rubber-like, underwater superoleophobic hydrogel for efficient oil/water separation," *Chemical Engineering Journal*, vol. 361, pp. 364–372, 2019.

[67] A. Tinti, A. Giacomello, and C. M. Casciola, "Vapor nucleation paths in lyophobic nanopores," *Eur. Phys. J. E: Soft Matter Biol. Phys.*, vol. 41, no. 4, p. 52, 2018.

[68] W. Ren, "Wetting transition on patterned surfaces: transition states and energy barriers," *Langmuir*, vol. 30, no. 10, pp. 2879–2885, 2014.

[69] E. S. Savoy and F. A. Escobedo, "Molecular simulations of wetting of a rough surface by an oily fluid: Effect of topology, chemistry, and droplet size on wetting transition r ates," *Langmuir*, vol. 28, no. 7, pp. 3412–3419, 2012.

[70] E. S. Savoy and F. A. Escobedo, "Simulation study of free-energy barriers in the wetting transition of an oily fluid on a rough surface with reentrant geometry," *Langmuir*, vol. 28, no. 46, pp. 16080–16090, 2012.

[71] M. Amabili, A. Giacomello, S. Meloni, and C. M. Casciola, "Collapse of superhydrophobicity on nanopillared surfaces," *Phys. Rev. Fluids*, vol. 2, no. 3, p. 034202, 2017.

[72] L. Guillemot, T. Biben, A. Galarneau, G. Vigier, and É. Charlaix, "Activated drying in hydrophobic nanopores and the line tension of water," *Proc. Natl. Acad. Sci. U.S.A.*, vol. 109, no. 48, pp. 19557–19562, 2012.

[73] E. Bormashenko and G. Whyman, "On the role of the line tension in the stability of cassie wetting," *Langmuir*, vol. 29, no. 18, pp. 5515–5519, 2013.

[74] L. Wang, R. Wang, J. Wang, and T.-S. Wong, "Compact nanoscale textures reduce contact time of bouncing droplets," *Science advances*, vol. 6, no. 29, p. eabb2307, 2020.

[75] J. Wang, Y. Wu, Y. Cao, G. Li, and Y. Liao, "Influence of surface roughness on contact angle hysteresis and spreading work," *Colloid Polym. Sci.*, vol. 298, pp. 1107–1112, 2020.

[76] M. Yan, T. Li, P. Zheng, R. Wei, Y. Jiang, and H. Li, "Wetting state transition of a liquid gallium drop at the nanoscale," *Phys. Chem. Chem. Phys.*, vol. 22, no. 21, pp. 11809–11816, 2020.

[77] D. Quéré, "Wetting and roughness," *Annu. Rev. Mater. Res.*, vol. 38, pp. 71–99, 2008.

[78] M. A. Gondal, M. S. Sadullah, M. A. Dastageer, G. McKinley, D. Panchanathan, and K. K. Varanasi, "Study of factors governing oil–water separation process using tio2 films prepared by spray deposition of nanoparticle dispersions," *ACS applied materials & interfaces*, vol. 6, no. 16, pp. 13422–13429, 2014.

[79] Y. Liu, K. Zhang, W. Yao, C. Zhang, Z. Han, and L. Ren, "A facile electrodeposition process for the fabrication of superhydrophobic and superoleophilic copper mesh for efficient oil–water separation," *Industrial & Engineering Chemistry Research*, vol. 55, no. 10, pp. 2704–2712, 2016.

[80] J. Joanny and P.-G. De Gennes, "A model for contact angle hysteresis," *The journal of chemical physics*, vol. 81, no. 1, pp. 552–562, 1984.

[81] M. Reyssat and D. Quéré, "Contact angle hysteresis generated by strong dilute defects," *The Journal of Physical Chemistry B*, vol. 113, no. 12, pp. 3906–3909, 2009.

[82] A. Giacomello, L. Schimmele, and S. Dietrich, "Wetting hysteresis induced by nanodefects," *Proceedings of the National Academy of Sciences*, vol. 113, no. 3, pp. E262–E271, 2016.

[83] Y. Zhang and W. Ren, "Numerical study of the effects of surface topography and chemistry on the wetting transition using the string method," *The Journal of Chemical Physics*, vol. 141, no. 24, p. 244705, 2014.

[84] S. C. Thickett, C. Neto, and A. T. Harris, "Biomimetic surface coatings for atmospheric water capture prepared by dewetting of polymer films," *Advanced Materials*, vol. 23, no. 32, pp. 3718–3722, 2011.

[85] Y. Guo, X. Zhao, F. Zhao, Z. Jiao, X. Zhou, and G. Yu, "Tailoring surface wetting states for ultrafast solar-driven water evaporation," *Energy & Environmental Science*, vol. 13, no. 7, pp. 2087–2095, 2020.

[86] B. Becher-Nienhaus, G. Liu, R. J. Archer, and A. Hozumi, "Surprising lack of influence on water droplet motion by hydrophilic microdomains on checkerboard-like surfaces with matched contact angle hysteresis," *Langmuir*, vol. 36, no. 27, pp. 7835–7843, 2020.